THESIS

THE DEVELOPMENT AND IMPLEMENTATION OF A HYBRID ROCKET MOTOR THRUST STAND TO INVESTIGATE THE RELATIONSHIP BETWEEN COMBUSTION CHAMBER PRESSURE AND GRAPHITE ROCKET NOZZLE EROSION IN HYBRID ROCKET MOTORS

Submitted by

Matthew Kronwall

Department of Mechanical Engineering

In partial fulfillment of the requirements

For the Degree of Master of Science

Colorado State University

Fort Collins, Colorado

Fall 2022

Master's Committee:

Advisor: Bret Windom

Anthony Marchese
Seonah Kim

ABSTRACT

THE DEVELOPMENT AND IMPLEMENTATION OF A HYBRID ROCKET MOTOR THRUST STAND TO INVESTIGATE THE RELATIONSHIP BETWEEN COMBUSTION CHAMBER PRESSURE AND GRAPHITE ROCKET NOZZLE EROSION IN HYBRID ROCKET MOTORS

Rocket motors frequently implement carbon-based nozzle inserts to insulate the motor from the heat produced by combustion. Over time these inserts will erode due to oxidation at the surface wherein oxidizing species found in the combustion products react with the carbon to form carbon monoxide. It has been shown that the largest contributors/oxidants to erosion are H2O, CO2, and OH, due to their high concentrations within the exhaust products and the low activation energy needed to react with the carbon surface. As such, a clear understanding of the rate of oxidation, or erosion, is critical to rocket motor design. Previous research has modeled many of these characteristics, yet this has largely been limited to solid rocket motors with combustion chamber pressures greater than 6.9 MPa. Earlier studies have asserted that combustion chamber pressure has a linear effect on erosion rates, but it is unclear whether this linear assumption can be extrapolated to lower chamber pressures. This research lays the foundational work to explore the relationship between combustion chamber pressure and erosion rates at pressures below 6.89 MPa. Based on the numerical modeling and rocket motor test firings described in this study, preliminary findings indicate that this linear assumption may not hold at combustion chamber pressures below 3.4 MPa.

Initial numerical modeling shows a non-linear increase in boundary layer thicknesses as combustion chamber pressures fall below 3.4 MPa. It is postulated that thicker boundary layer

slows the diffusion of the oxidizing species to the surface thereby decreasing the rate of erosion. Thus, the modeled results suggest a non-linear relationship between nozzle erosion and pressure may be present at lower chamber pressures. Moreover, pure hydrocarbon fuels generate high fractions of key oxidizing species (H2O, CO2, and OH) in the product stream and the impact of these fuels on carbon nozzle erosion has remained largely unexplored. A hybrid rocket motor test stand (HRMTS) was developed to perform test fires of a HTPB-N2O hybrid motor at chamber pressures between 2.07 MPa and 4.83 MPa. Supplementary research was carried out that explored hybrid motor injectors and their effects of combustion instabilities. Major milestones included, implementation of a new semi-autonomous LabVIEW VI, creation of a MATLAB model that predicts motor performance, design and manufacture of a modular hybrid rocket motor, and the development of a secondary model that uses gathered test data to predict transient throat diameters. Furthermore, the predicted nozzle erosion was validated with the measured nozzle surface geometry pre and post-test fire through the utilization of a coordinate measuring machine (CMM). Initial results show that, despite the non-linear boundary layer growth, a linear relationship between combustion chamber pressure and nozzle erosion may still be true for chamber pressures below 6.89 MPa. Testing also illuminated correlations between combustion stability with injector pressure and nitrous oxide phase, for which, poor oxidizer vaporization and injector pressure dramatically decrease combustion stability and motor performance.

ACKNOWLEDGEMENTS

I would firstly like to acknowledge and thank my advisors, Dr. Bret Windom, Dr. Anthony Marchese, and Dr. Seonah Kim, for offering their time to be on my committee. Your patience and input have been invaluable to this project and my sanity. In the beginning of this research, I found myself intimidated and often paralyzed by the challenges ahead. I am no less intimidated now, but I would not have been able to understand my potential without being given the responsibility of such a large project and I no longer fear the challenges ahead.

A huge thank you to everyone at the Powerhouse, in particular those Chemical Energy Conversion Lab (CECL). Despite this research taking me all over town, I have never felt like a stranger and have always been welcomed with open arms. I will never forget the classes we took together and the fun we had. Thank you to Kirk Evans and all incites regarding LabVIEW, without you I would still be beating my head against my keyboard.

When my research moved across town to the Engineering Research Center, I was greeted with equally open arms, especially Seth Thompson and everyone at the CSU Electric Propulsion & Plasma Engineering (CEPPE) Lab. The work of Karl Swanson and Chris Giglio at Colorado State University Environmental Health Services cannot be understated. Their time and effort have not gone unnoticed. Thank you for helping me accomplish my one goal, don't blowup.

Were it not for the inspiration from Dr Robert Zubrin and Pioneer Astronautics this research would not have been possible. Additionally, the equipment loaned to CSU from Sierra Nevada Corporation was the backbone of this research and for that I am truly grateful. Thank you to James Wilson and Manes Machine & Engineering Company for providing access to invaluable equipment and time.

On a more personal note, I am so grateful for all the amazing supportive friends I have made in the last few years. Thank you to my parents for their continued support though my academic career. A special thanks to Susan Ossareh, Sean Hershfeldt, and Nick Brunson-Williams. They all provided me with overwhelming support and advice throughout my time at Colorado State University and have changed my life in profound ways. Most importantly, I want to thank my partner Dr. Jennie Bukowski for her continued support, guidance, and perspective throughout my masters. Thank you for being the funniest person I know.

My time at Colorado State University has very much embraced the phrase, “it takes a village.” I have had the wonderful opportunity to work with some of the most talented people I have ever met. And to all those I say thank you.

TABLE OF CONTENTS

LIST OF TABLES

LIST OF FIGURES

CHAPTER 1 - INTRODUCTION

1.1 Motivation

The increased demand for smaller, more affordable, rocket motors has caused ablative nozzles, or nozzle inserts, to be a compelling solution to simplify nozzle design without sacrificing motor integrity. Traditionally, nozzle cooling has been divided into two categories, active and passive cooling. Active cooling, or regenerative cooling, implements a heat exchanger to cool the nozzle and combustion chamber by passing liquid fuel through a series of channels before entering the injector. The primary benefits of active cooling are an overall increase in combustion efficiency due to pre-heating the fuel before entering the combustion chamber and increasing the longevity of the nozzle considerably [1]. Nevertheless, these systems dramatically increase complexity and weight when compared to their passive counterpart. Passively cooled nozzles generally consist of a carbon-based liner or insert pressed into the nozzle acting as a protective barrier. During combustion, the surface material will vaporize and maintain a constant nozzle temperature due to heat lost through mass transfer, a process referred to as ablation [2], [3]. Importantly, ablation is a chemical process; the nozzle will erode over time, which directly affects the performance of the motor. Despite the decreases in performance, passive solutions have historically been the go-to when safety and reliability are the largest concerns, with the best examples being the Lunar Lander and the Apollo Service Module.

Fundamentally, a rocket nozzle produces thrust by choking the flow of exhaust gases through a converging-diverging nozzle. The converging section compresses and accelerates the exhaust gas to Mach one, forming a standing shockwave between the converging and diverging sections, known as the throat. Beyond the shockwave, the fluid decreases in density, accelerating the flow. This effect compounds as the nozzle diverges, further expanding the gas supersonically,

reaching velocities that exceed Mach two. This means that the thrust is directly controlled by the upstream pressure generated within the combustion chamber and the mass flow rate through the throat. Here, the mass flow rate of the motor can be considered constant and therefore as the throat diameter increases the combustion chamber pressure will decrease. This reduces the fluid velocity at the end of the nozzle and in turn, decreases the overall thrust. Simply put, nozzle ablation decreases motor performance [1]. Figure 1 shows the decrease in motor performance caused by a 25% increase in throat diameter. In this simplified case, where the mass flow rate is held constant, the chamber pressure decreases by roughly 35%, causing a decrease in thrust of about 6.5%. This may not seem substantial, but fuel capacity requirements are an exponential function, meaning that a 6.5% decrease in thrust requires 18% more fuel. In small cases, differences in fuel capacity may only amount to several kilograms, yet when considering long-distance missions to Mars or the Moon, those differences may be thousands of kilograms. Moreover, nozzle erosion affects more than just chamber pressure. Rather, it creates multiple feedback loops affecting combustion energetics and injector performance. Also, ablative nozzle inserts are often structural elements and if unchecked, excessive nozzle erosion may lead to mechanical failures in addition to failures related to engine performance. As such, understanding the mechanisms that control erosion and the rate of erosion are critical to successful engine design.

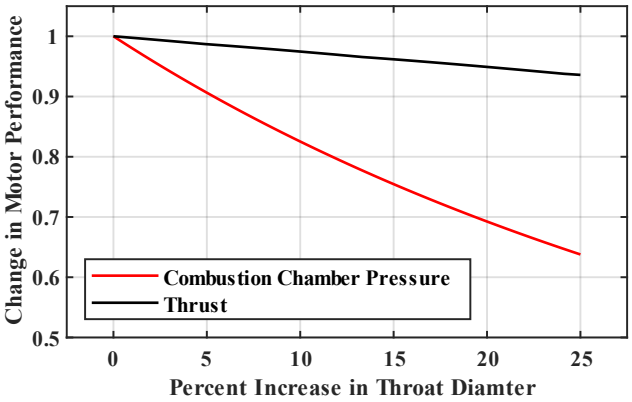

Figure 1. A representation of the decreased motor performance due to increasing throat diameter.

1.2 Chemical Erosion

There are three main types of chemical rocket motors, with each being functionally similar. Chemical propellants can be categorized as either solid or liquid with the types of motors being the different combinations of the two propellants: “Solid” motors, “liquid” motors, and a “hybrid” of the two. Solid motors, as the name suggests, use both a solid oxidizer and solid fuel, wherein a powderized oxidizer, such as ammonium perchlorate (AP), is suspended in a solid binder, often hydroxyl terminated polybutadiene (HTPB) - a substance very similar to rubber. Powdered metals can be added to solid fuel to increase combustion energetics, the most common of which is aluminum, and to a lesser extent iron and magnesium [1], [4]. Solid motors suffer from low performance but are overwhelmingly the cheapest and simplest motor design. Yet, solid rocket motors are still the preferred choice for both military and research applications, despite the decreased performance.

Similarly, liquid motors use a liquid fuel and liquid oxidizer with the most common examples being RP-1, or kerosene, and liquid oxygen. Liquid motors are the most efficient, yet they are more complex and costly compared to the other motor types. Often requiring significantly

more infrastructure for testing and therefore much less common outside of large-scale commercial operations.

The last type uses the solid fuel grain found in solid motors in conjunction with the liquid oxidizer found in liquid motors to create a hybrid of the two motors, hence the name “hybrid”. These motors maintain the relative simplicity of solid motors while exhibiting a similar increase in performance to liquid motors [1]. While extra infrastructure is necessary for testing hybrid systems, the increased complexity is still less than that required to test liquid motors. Hybrids come with their own set of challenges, like combustion instabilities, which will become apparent later in this study.

With regards to erosion, the critical distinction between the three motor types is fuel chemistry. It has been shown that erosion is directly related to the concentrations of oxidizing species within the exhaust products, with the highest contributors being H_2O, CO_2, and OH [5]-[8]. Since solid motors use a solid oxidizer alongside metal additives, the overall concentrations of oxidizing species decrease due to the formation of metal oxides. The inverse is true for both liquid and hybrid motors, so long as metal additives are not added to the fuel grain. Because the fuels consist of only hydrocarbons, the combustion process will produce more H_2O, CO_2, and OH rather than forming metal oxides like those found in solid rocket motors. Thus, liquid and hybrid motors will experience more erosion compared to solid motors. In fact, H_2O concentrations in liquid motors can be almost twice that of solid motors, with CO_2, and OH concentrations three to five times higher and upwards of eight times higher in some cases.

To clarify, nozzle erosion is the result of oxidation at the nozzle surface, where an oxidizing species interacts with the nozzle wall and subsequently strips a carbon from the surface to form CO. Reactions (1), (2), and (3) demonstrate this with regards to H_2O, CO_2, and OH. Note that any

molecule with an oxygen atom may react with the nozzle, but because the relative concentration of H_2O and CO_2 is much higher than that of more reactive species, H_2O and CO_2 will contribute more to erosion overall.

$$C_{(s)} + H_20 \rightarrow CO + H_2 \quad (1)$$

$$C_{(s)} + CO_2 \rightarrow 2CO \quad (2)$$

$$2C_{(s)} + 2OH \rightarrow 2CO + H_2 \quad (3)$$

One of the major obstacles with ablative nozzles is that minimizing the rate of these reactions is difficult. Carbon materials, most commonly carbon phenolic or graphite, are implemented because they are naturally resistant to high temperatures and will maintain structural integrity in extreme conditions [11]. Other materials, such as sintered metals, have also shown promise, but thermal shock during motor startup often causes cracking, leading to mechanical failures [9]. Therefore, softer materials, like carbon, are more frequently used despite being much more susceptible to erosion. That is, softer materials require less energy or surface temperature for reactions to occur. For which, carbon begins to react at 1500K compared to the 3000K needed for sintered metals [10]. This also means that erosion will not occur immediately, but only after the nozzle reaches the associated wall temperatures.

Consequently, erosion will occur at and just behind the throat due to the combination of high pressure and temperature alongside the smallest boundary layer compared to the rest of the engine. Because erosion is a chemical process, the diffusion and mass transfer of oxidizing species to the nozzle wall becomes relevant [12]. As such, chamber pressure affects erosion rates, with erosion increasing as chamber pressure increases [8]-[10], [12], [13]. Likely, this is due to the relationship between boundary layer thickness and chamber pressure [12]. As pressure increases,

the boundary layer and subsequent diffusion length decrease, which increases the mass transfer to the wall, thereby increasing erosion rates. Studies suggest combustion chamber pressure has a linear effect on erosion rates, as seen in Figure 2. Nevertheless, this work has largely been limited to chamber pressures above 6.9 MPa [13], [14]. However, there is some research showing non-linear boundary layer growth at lower pressures when examining hybrid motor fuel grain regression [15], meaning that the boundary layer thickness increases more rapidly as the pressure drops below 1.72 MPa. This phenomenon can likely be applied to other boundary-dependent effects, like those in the throat, suggesting that pressure may have a greater effect on erosion rates below 6.9 MPa due to the non-linearity of the boundary layer.

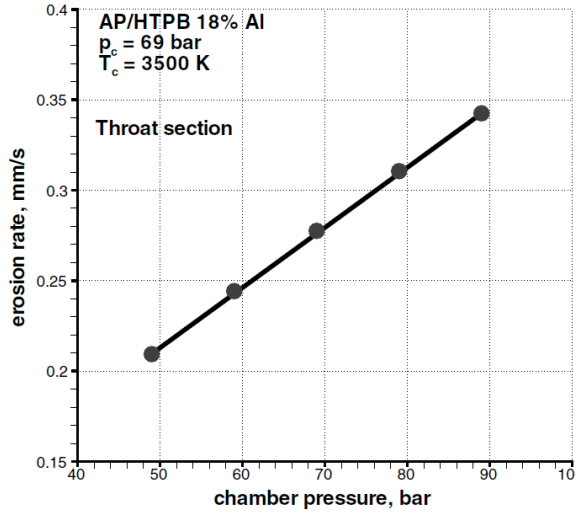

Figure 2. Taken from Bianchi et al. [14]: Previous research depicting a linear increase in erosion in solid rocket motors.

Furthermore, previous research has focused on solid rocket motors comprised of hydroxyl-terminated polybutadiene (HTPB), ammonium perchlorate (AP), and aluminum. As mentioned, this has a notable effect on nozzle erosion due to the combustion composition. Moreover, aluminum content within the fuel has been directly tied to decreased erosion rates not only because of the formation of Al_2O_3, but also due to a process called aluminization within throat.

Aluminization is a mechanical process where unburned molten aluminum creates a protective barrier on the nozzle wall that resists further oxidation [8], [9], [16], [17]. As such, much of the current data cannot be directly applied to motors other than solid rocket motors. Even though a one-to-one comparison between multiple fuel types is unrealistic, strides can still be made to understand the underlying causes of erosion.

1.3 Preliminary CFD Modeling

Much of the motivation for this project originated in a collaboration with Pioneer Astronautics to determine heat transfer and cooling requirements within a proposed ethene and nitrous oxide motor operating below 1.38 MPa. Both ablative and regenerative methods were pursued, including a promising dual-channel regenerative nozzle. Ablative solutions, on the other hand, lacked the data needed to determine erosion rates for the proposed fuel composition and combustion chamber pressures [18]. Current carbon nozzle erosion rate predictions range anywhere from 0.09 mm/s to rates exceeding 0.35 mm/s [3], [8], [9], [17]. This leads to ambiguity surrounding the accuracy of erosion rates when extrapolated to lower pressures. Simultaneously, preliminary modeling showed non-linear boundary layer growth as the chamber pressure increased, demonstrated in Figure 3.

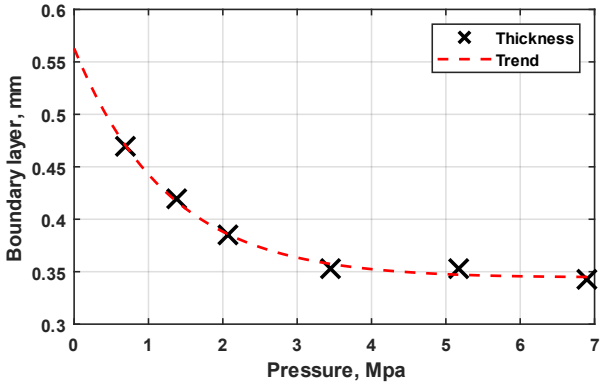

Figure 3. Modeled boundary layer thickness at various combustion chamber pressures with an exponential trend between data points.

The modeling work for motivating this project employed Ansys Fluent and the National Aeronautics and Space Administration (NASA) Chemical Equilibrium with Applications (CEA) Code to construct and simulate operating conditions within the rocket nozzle [19]. Simulations were run at combustion chamber pressures between 0.69 MPa and 6.9 MPa to calculate the change in boundary layer thickness at the throat, demonstrating a non-linear relationship between boundary layer growth and chamber pressure (Figure 3). A quasi-linear relationship was documented at pressures above 3.4 MPa, with a transitional region depicting non-linear characteristics below 3.4 MPa. This indicates that linear extrapolation of erosion rates may not be valid for pressures below 3.4 MPa.

1.4 Overview and Objectives

Based on the limitations of previous literature and the initial modeling results, the need for more data on erosion rates is clear, especially in the case of low pressure rocket motors that exclusively use hydrocarbon fuels. While the idealized Ansys Fluent simulations suggested a non-linear relationship between erosion rates for low combustion chamber pressures below 3.4 MPa, this hypothesis needed to be tested practically and real data needed to be collected from a physical hybrid rocket motor system. However, the rocket motor design, testing infrastructure, and data

collection systems necessary to test this hypothesis were nonexistent. *Therefore, the main goal of this project is to design and construct a rocket motor testbed that allows us to collect data on erosion rates at low chamber pressure and evaluate the validity of the hypothetical non-linear relationship between these two variables.*

To begin, this research was conducted using a thrust stand loaned to Colorado State University (CSU) by Sierra Nevada Corporation. The thrust stand was designed to run hybrid rocket motors using liquid nitrous oxide (N_2O) as an oxidizer, referred to as the Hybrid Rocket Motor Thrust Stand (HRMTS). Much of this project centered on modernizing and repairing this equipment to establish a long-lasting and reliable piece of equipment for continued research surrounding hybrid rocket motors. There were three major objectives, which include: (1) developing the HRMTS to reliably capture motor performance, (2) designing and manufacturing a modular HTPB-N_2O hybrid rocket motor capable of operating at multiple chamber pressures, which subsequently included injector designs specific to hybrid rocket motors, and (3) testing three different chamber pressures within the transition region to capture any non-linear characteristics. This last goal also included data analysis that would correlate measured motor performance to the measured nozzle erosion.

The experiment was set up to implement HTPB-N_2O hybrid rocket motors with a total burn time of 30 seconds for each test. Design plans started with a motor that operates at 2.07 MPa and produces 1.11 kN of thrust before moving on to the other motor designs. Because of this, much of the design, most notability the nozzle geometry, was established by the 2.07 MPa motor design and then carried over to the later iterations. Since the 2.07 MPa motor design was the first motor tested, a large margin for safety was required. The exact limitations of the HRMTS will be discussed in more detail later, but for now, understand that 2.07 MPa falls well below these

limitations. Nevertheless, lowering the combustion chamber pressure too much has also been recognized to induce combustion instabilities, with the limit being near 1.74 MPa [15]. Hence, 2.07 MPa was selected as it met the previous criteria and was also within the transition region shown in Figure 3. Later tests were performed at 3.45 MPa and 4.83 MPa, one centered in the transition region with the other at the high end of the transition. Note that the chamber pressure is limited to 4.83 MPa due to inherent limitations in the thrust stand.

HTPB and nitrous oxide were selected as the fuel and oxidizer because of their availability, widespread industry use, and because they have been previously researched. Importantly, nitrous oxide is preferred due to the relatively low pressures and temperatures needed to maintain a liquid state, removing the need for cryogenics. Finally, graphite was chosen as the nozzle material due to similar cost and availability needs, but also because it has a uniform grain structure. This means that the surface reactions only include carbon and simplify the potential reactions compared to other common materials such as phenolic. Each nozzle was measured pre- and post-burn to accurately measure erosion. Post-burn nozzle geometry was then correlated to motor conditions measured during testing and the subsequent erosion rate based on thrust, combustion chamber pressure, and the oxidizer to fuel ratio (O/F) was calculated.

CHAPTER 2 - HYBRID MOTOR DESIGN

2.1 General Rocket Motor Design Theory

Fundamentally, all chemical rocket motors function the same. That is, fuel and oxidizer is consumed to produce pressure within a combustion chamber, forcing hot gases through a converging-diverging nozzle to produce thrust. Specifically, thrust, F, is proportional to the mass flow rate through the nozzle, $\dot{m}$, and the fluid velocity at the exit of the nozzle, u_{exit}, expressed in Equation 4. This can be expanded because the exit velocity is related to the nozzle expansion and the combustion process within the combustion chamber. Therefore, it is beneficial to separate the combustion process and the thrust produced by the nozzle expansion. The combustion energetics are represented by the characteristic velocity, or C^*, with the nozzle characteristics represented by the thrust coefficient, C_F. In practical terms this means that thrust is defined by the mass flow rate through the nozzle, the characteristic velocity, and the thrust coefficient (Eqn. 5).

$$F = \dot{m}\, u_{exit} \tag{4}$$

$$F = \dot{m}\, C^*\, C_F \tag{5}$$

Again C^* and C_F can be defined practically, with the characteristic velocity defined by the combustion chamber pressure, P_C, mass flow rate, and nozzle throat area, A_t, (Eqn. 6) and the thrust coefficient defined by the motor thrust, combustion chamber pressure, and throat area (Eqn. 7). This has the added benefit that the motor performance, and by extension the exit velocity, can be determined by easily measurable properties. Equations 6 and 7 also demonstrate why the throat area becomes important, showing that both combustion properties and nozzle properties are directly related to the nozzle throat area.

$$C^* = \frac{P_C\, A_t}{\dot{m}} \tag{6}$$

$$C_F = \frac{F}{P_C A_t} \tag{7}$$

Moreover, since the combustion process and nozzle characteristics are decoupled, each can be defined by the processes occurring within their respective areas. That is, C^* is derived through the thermodynamic properties determined by the combustion reactants and pressure, and C_F is derived by the isentropic Mech relations. Both derivations assume that the fluid acts as an ideal gas and the processes are isentropic, thereby making both equations heavily dependent on the ratio of specific heats, γ. Both derivations start at the throat where the Mech number is known to one, but differ in that the characteristic velocity is related to the stagnation pressure and the thrust coefficient is defined by the exit pressure. In essence C^* is defined by moving from the throat inward and C_F is defined by the throat moving outward. This all results in Equations 8 and 9 [1].

$$C^* = \frac{1}{\sqrt{\gamma}\left(\frac{2}{\gamma-1}\right)^{\frac{\gamma+1}{2(\gamma-1)}}} \sqrt{\frac{\bar{R}\, T_A}{MW}} \tag{8}$$

$$C_F = \sqrt{\gamma}\left(\frac{2\gamma}{\gamma+1}\right)^{\frac{\gamma+1}{2(\gamma-1)}} \sqrt{\left(\frac{2\gamma}{\gamma-1}\right)\left(1-\left(\frac{P_e}{P_c}\right)^{\frac{\gamma-1}{\gamma}}\right)} + \left(\frac{A_{exit}}{A_t}\right)\left(\frac{(P_{exit}-P_{amb})}{P_c}\right) \tag{9}$$

Other nuances include C^* being defined as a constant pressure adiabatic reactor related to the local speed of sound at the throat, making it a function of the universal gas constant, $\bar{R}$, molecular weight at the throat, MW, and the adiabatic flame temperature, T_A. Subsequently, all of these properties are determined by oxidizer and fuel enthalpies of formation, and chemical equilibrium prior to the throat. Importantly, the enthalpies of formation are heavily dependent on the mixer ratio of the fuel and oxidizer, which is referred to as the oxidizer to fuel (O/F) ratio.

C_F, on the other hand, uses the pressure ratio, the ratio between the nozzle exit pressure and the combustion chamber pressure, P_e/P_C, as well as the ratio between the nozzle throat area and nozzle exit area, or area ratio, A_{exit}/A_t, to calculate the expansion of the exhaust gas. This

specifically defines the contribution of the nozzle expansion to the overall thrust. Importantly, optimal operating conditions occur when the exit pressure is equal to the ambient pressure. As such, an additional term is added to C_F that takes in to account any contributions or hindrances caused by ambient pressure changes, P_{amb}, which primarily arise when the ambient pressure decreases as a rocket gains altitude. Moreover, the thrust coefficient is related to the ratio of specific heat is affected by changes in the exhaust product composition, albeit weakly.

The last important design parameter is the area ratio found in Equation 9. The area ratio, or the ratio of cross-sectional areas of the throat and nozzle exit, dictates the gas expansion and governs the nozzle exit pressure. The area ratio is derived using the same assumptions as the thrust coefficient and combines aspects from both the characteristic velocity and the thrust coefficient to produce a variable only in terms of the pressure ratio and γ (Eqn. 10)[1].

$$\frac{A_{exit}}{A_t} = \frac{\sqrt{\gamma}\left(\frac{2}{\gamma+1}\right)^{\frac{\gamma+1}{2(\gamma-1)}}}{\left(\frac{Pe}{Pc}\right)^{\frac{1}{\gamma}}\sqrt{\left(\frac{2\gamma}{\gamma-1}\right)\left(1-\left(\frac{Pe}{Pc}\right)^{\frac{\gamma-1}{\gamma}}\right)}} \tag{10}$$

In Summary, Equations 8, 9, and 10, make it possible to define each aspect of the motor. Thrust, chamber pressure, and exit pressure are easily definable motor parameters during the design process. The only exception is the ratio of specific heats, due to its dependance on chemical composition. Nevertheless, γ can initially be assumed, typically starting at 1.2, then iterated to achieve the ideal exit pressure once more combustion characteristics are known.

2.2 Hybrid Motor Design

Hybrid motor design presents unique challenges compared to solid and liquid motors, mainly related to combustion. This is because the fuel and oxidizer exist in two different states. Unlike liquid rocket motors that rely heavily on propellant mixing, or solid motors where the

oxidizer is premixed within the fuel grain, hybrid motors rely on diffusion of oxidizer to the fuel grain surface (Figure 4) [20], [23].

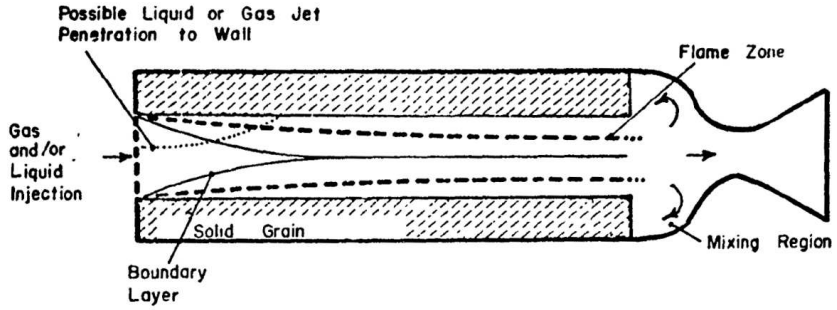

Figure 4. Taken from Netzer and Bae [20]: General anatomy of a hybrid rocket motor.

During combustion, fuel is vaporized at the surface through convective and radiative heat transfer. At which point, the vaporized fuel then mixes with oxidizer traveling parallel to the fuel grain and combusts. This type of combustion produces what is called a turbulent diffusion flame, whereby a standing flame is produced and sits above the fuel grain where stoichiometric mixing is reached. As the name suggests, this is a process related to diffusion where oxidizer must first diffuse toward the fuel grain before combustion can occur. This also means that the rate of combustion is related to the fuel vaporization. As the fuel vaporizes, mass is transferred into the flame, consuming the fuel grain and causing it to regress. The consumption, or regression, of the fuel is governed by the total oxidizer mass flux across the fuel grain, typically measured in meters per second. Equation 11 shows this relationship where $\dot{r}$ is the regression rate, G_o is the oxidizer mass flux across the fuel grain, and a and n being experimentally derived coefficients [1], [20]-[23].

$$\dot{r} = aG_o{}^n \tag{11}$$

Although, the actual combustion of solid fuel is extremely complex and depends on processes such as heat penetration, the rate of char layer formation, and particle entrainment, the

simplicity of Equation 11 often does an adequate job predicting regression rates [1], [21], [22]. Nevertheless, a and n are highly dependent on fuel and oxidizer combinations, combustion chamber pressure, and combustion efficiency, which can lead to discrepancies between test fires. The mass flow rate of the fuel can then be calculated by combining the regression rate in combination with the fuel density, ρ_f, and the total surface area of the fuel grain or burn area, A_b, (Eqn. 12). Grain geometries can come in a wide range of shapes, but it has been simplified here to a single cylinder so that the burn area only regress as a function of the radius (Eqn. 13).

$$\dot{m}_f = \rho_f \, \dot{r} \, A_b \tag{12}$$

$$A_b = \pi \, {r_{grain}}^2 \, L \tag{13}$$

Nevertheless, radial diffusion must be considered alongside axial diffusion. As oxidizer is consumed, the combusting gas will become increasingly fuel rich further down the fuel grain. This results in an oxidizer rich region toward the injector and a fuel rich region toward the nozzle, leading to incomplete combustion at either end. This in turn reduces the flame temperature and combustion chamber pressure as the O/F ratio moves away from stoichiometric. This ultimately produces a feedback loop because the changing O/F ratio would reduce the regression rate and combustion efficiency, further reducing chamber pressures until a new equilibrium is reached. This process has also been shown to contribute to combustion instabilities, which would further exacerbate these fluctuations [24], [26]. Fortunately, it has been shown that an optimal length to diameter ratio (L_{grain}/D_{grain}), the relationship between overall length of the fuel grain and grain port diameter, can reduce these instabilities and inefficiencies and typically range from 10 to 12 [24].

2.3 Injector and Oxidizer Mass Flow Rate

The second half of motor design is related to the oxidizer mass flow rate and by extension, injector design. To start, the oxidizer mass flow rate is proportional to the pressure gradient between the combustion chamber and the pressure upstream of the injector, or tank pressure. To further simplify, Bernoulli's equation can be implemented by assuming the flow through the injector remains incompressible, assuming the mass flow rate remains constant, and that gravitational effects are negligible (Eqn. 14 and 15).

$$P_{in} + \frac{1}{2}\rho_{in}{u_{in}}^2 = P_{out} + \frac{1}{2}\rho_{out}{u_{out}}^2 \tag{14}$$

$$\dot{m} = \rho_{in}u_{in}A_{in} = \rho_{out}u_{out}A_{out} \tag{15}$$

Since the fluid is assumed to be incompressible, density remains constant. Moreover, upstream of the injector inlet can be treated to be a plenum, and as such $A_{in} \gg A_{out}$. Therefore, Equations 14 and 15 can be simplified to produce Equation 16. This makes the oxidizer mass flow rate proportional to the total cross-sectional area of the injector ports (A_{inj}), fluid density (ρ_{oxi}), and the pressure gradient between the tank pressure, P_{tank}, and the combustion chamber pressure.

$$\dot{m}_{oxi} = C_d A_{inj}\sqrt{2\rho_{oxi}(P_{tank} - P_c)} \tag{16}$$

A discharge coefficient, C_d, is subsequently added to simplify the complex fluid interactions experienced within the injector ports and to account for viscous forces and compressibility. Under ideal circumstances, C_d would equal 1. However, the discharge coefficient it is highly dependent on injector port geometry and fluid properties. Therefore, the discharge coefficient is approximated from previous work and adjusted through experimentation.

2.4 Motor Design and Transient Model

From the test parameters discussed above, a MATLAB model was developed to determine the physical design requirements alongside transient motor performance and oxidizing processes within the exhaust products. The model implements thermodynamic properties gathered from the NASA CEA Code at the prescribed chamber pressures to determine nozzle expansion ratios, initial mass flow rates, and thrust. By maximizing C^* and specific impulse, a parameter that describes motor effectiveness, an optimal O/F ratio was determined to be 6. The model then calculates the fuel grain dimensions based on the desired O/F ratio and the L_{grain}/D_{grain} ratio. To that end, the model first calculates the O/F ratio at 7 rather than 6 because the surface area of the fuel grain will increase as the fuel is consumed and the grain regresses. Since the mass flow rate of the fuel is proportional to the burn area, the O/F ratio will drop over time. As such, the motor is designed to start oxidizer rich before reaching peak efficiency midway through the test. Here, 1.87e-4 and 0.347 are used for a and n in Equation 11 when calculating the fuel regression rate [28]. The transient portion of the model employs an implicit Euler solution method to determine the transient properties according to the new chamber pressure and oxidizer-fuel mass flow rates. See Figure 5 for the model flow diagram.

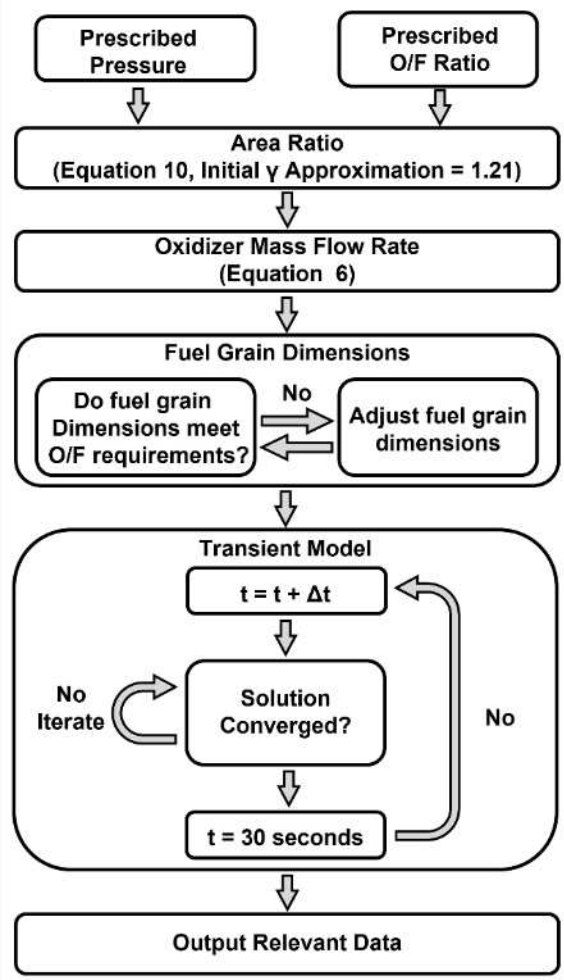

Figure 5. Motor model process flow diagram.

From the calculations conducted for the 2.07 MPa test, the nozzle was constructed with a throat diameter of 21.8mm and a 15-degree expansion angle (Figure 6). Note that the throat diameter remains constant throughout all tests with the only differences being the nozzle exit diameter. Consequently, the model was adjusted for subsequent cases where the throat area is fixed, and the mass flow rate is adjusted to account for the changes in combustion chamber pressures. The exact conditions for each case can be found in Table 1. Additionally, a 15-degree nozzle expansion angle has be shown to produce the desired expansion characteristics, contrasting the more aggressive and arbitrary 45-degree converging angle that has a much lower impact on nozzle performance [1]. Note that the thrust is only defined for the 2.07 MPa case. Since thrust is

a function of chamber pressure, throat area, and mass flow rate, and the mass flow rate is adjusted to compensate for the increased chamber pressure, the thrust then becomes an arbitrary value for later tests. While understanding thrust is necessary for data analysis it is not an important metric to consider during the design phase.

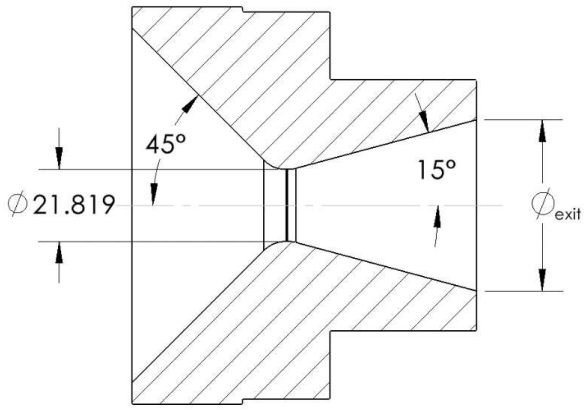

Figure 6. Cross-section of the nozzle with the standard dimension between all tests.

Table 1. Hybrid motor parameters at each desired chamber pressure.

Test #	P_C (MPa)	F (kN)	$\varnothing_{exit}$ (mm)	A_{exit}/A_t	$\dot{m}$ (kg/s)
1	2.07	1.14	44.5	4.17	0.48
2	4.83	2.84	58.6	7.21	1.12
3	3.45	1.98	51.9	5.66	0.80

Table 2. Concentrations of oxidizing species at each designed chamber pressure. All values were calculated at the throat with an O/F ratio of 6.

Test #	X_{CO}	X_{CO_2}	X_{H_2O}	X_{OH}	X_{O_2}	X_O
1	0.198	0.073	0.140	0.014	0.002	0.002
2	0.197	0.074	0.144	0.011	0.001	0.001
3	0.198	0.074	0.143	0.012	0.002	0.002

Figure 7 shows the predicted performance for the first, 2.07 MPa, case and illustrates many of the characteristics during the test fire. Although only one test case is shown, each modeled test

case shows similar tends, with only slight changes in O/F ratios. Figure 7 also shows the shift in O/F ratio discussed above, where the motor transitions from oxidizer rich to fuel rich. Furthermore, each case exhibits almost identical concentrations and behaviors related to the oxidizing species at the throat, wherein CO increases and CO_2 deceases, thereby reducing the primary contributor to erosion. This suggests that erosion will decrease as the O/F ratio shifts towards fuel rich.

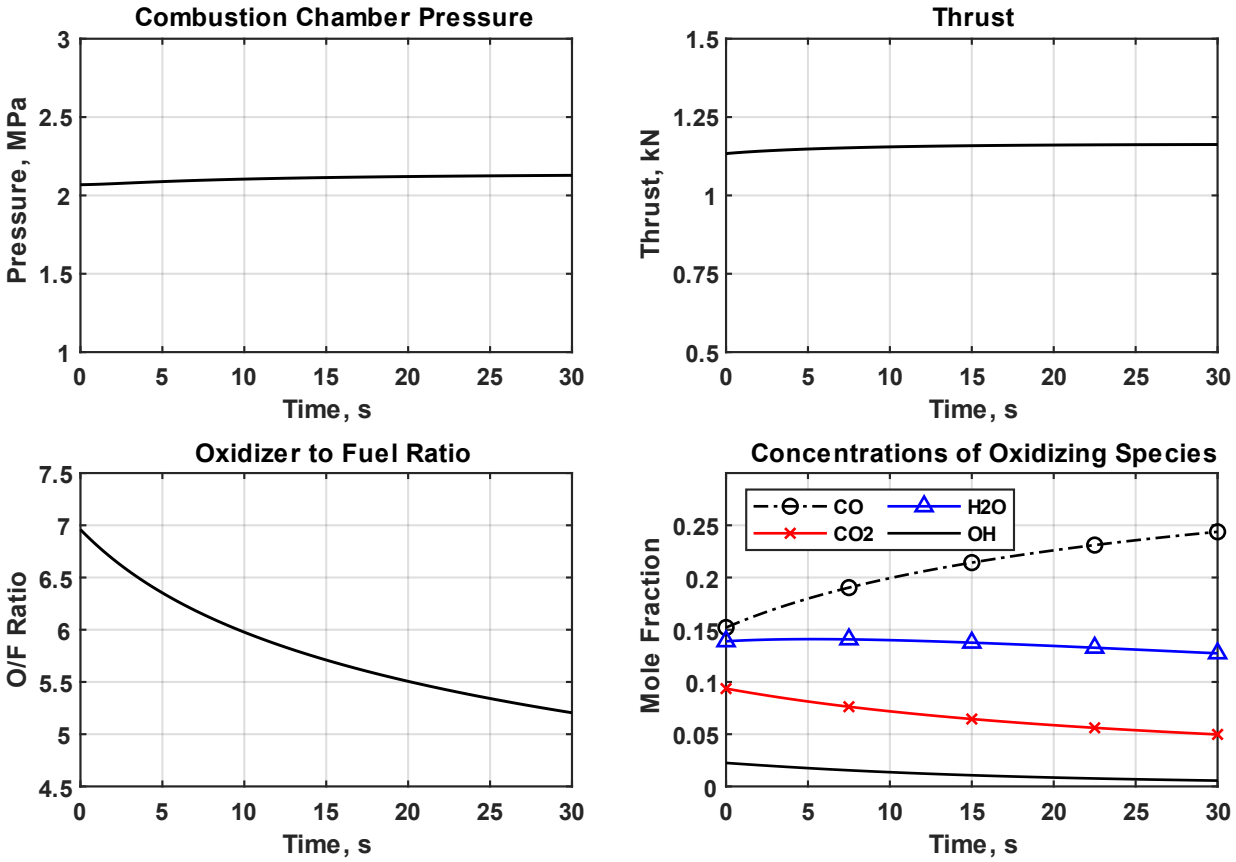

Figure 7. Predicated motor performance at 2.07 MPa for a 30 second burn duration.

2.5 Hybrid Rocket Motor Construction

The hybrid motor consists of three main sub-assemblies: the fuel grain, nozzle assembly, and rear bulkhead. The combustion chamber, or motor body, houses each assembly and acts as the main structural support. Both the front and rear of the motor body contains the primary and

secondary o-ring grooves that seal the motor casing, as well as snap ring grooves that hold the nozzle and rear bulkhead assemblies in place. Figure 8 shows the motor cross-section and highlights many of the key components.

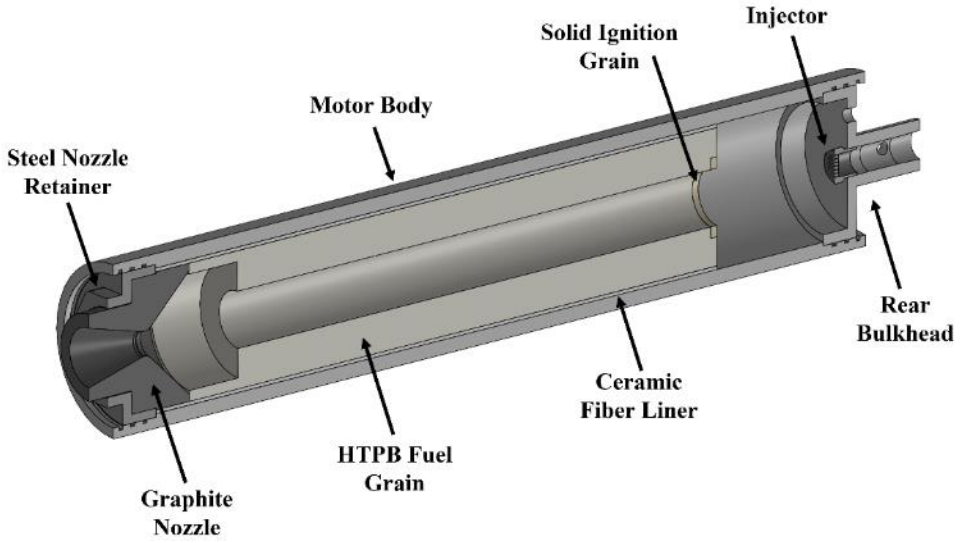

Figure 8. Cross-section of a hybrid motor design identifying key features.

Starting from the front and moving backward, the nozzle assembly is comprised of two parts: the graphite nozzle and a steel retainer. The steal retainer serves two purposes. First, the retainer adds additional structural support to the relatively brittle nozzle. Secondly, it acts as a heat spreader and thermal reservoir to spread the heat evenly across the o-rings during testing. Both the interior and exterior of the retainer are polished to facilitate sealing, yet a second o-ring is not used on the interior of the retainer because of graphite's natural ability to act as a gasket. Nevertheless, the nozzle is pressed firmly in place to ensure continuous sealing. Thermocouples are also placed along the motor exterior, one near the nozzle and rear bulkhead, with a third centered on the midpoint of the casing.

Moving inward, the HTPB fuel grain is surrounded by a ceramic fiber liner to help insulate the motor body. Conveniently, HTPB, or any solid fuel, also acts as an insulator due to the phase change occurring at the surface, which maintains a constant surface temperature around 900 K

[25]. However, the motor body would never reach 900 K since the heat would first need to conduct through the remaining HTPB. Nevertheless, the ceramic liner acts as a last line of defense, primarily insulating between the motor body and the nozzle. To that end, the motor body was designed to withstand 6.89 MPa at 200 C, 6.89 MPa being the max operation pressure of the thrust stand. At the rear of the fuel grain, a puck of solid fuel comprised of sucrose and potassium nitrate, is used to ignite the motor.

Lastly, the rear bulkhead contains the injector and sensor hardware. This includes two diaphragm pressure sensors that measure combustion chamber pressure and injector pressure. A thermocouple is positioned in front of the injector to measure the nitrous oxide temperature just before entering the injector. The injector is constructed from a modified 3/4 NPT plug and is threaded directly to the rear bulkhead. Figure 9 shows the exterior of the bulkhead and locations of the pressure sensors and thermocouple.

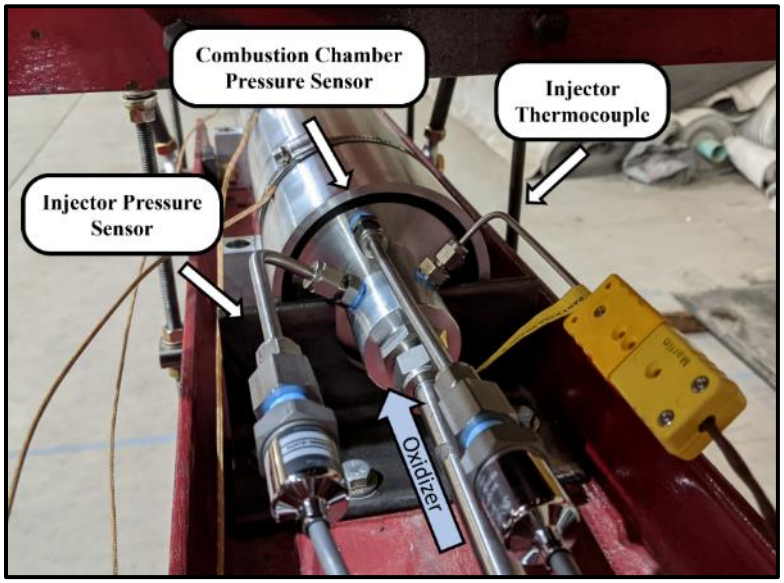

Figure 9. Photo identifying sensors attached to the rear bulkhead.

To reiterate, while maintaining a constant throat area, an increase in chamber pressure requires an increase in mass flow rate. To do so, the grain burn area must increase, which requires the fuel grain to lengthen. For that reason, a modularity design was implemented to facilitate changes in the fuel grain size, thus the motor casing was designed to accommodate the largest 4.83 MPa test. Nonetheless, a separate motor body was constructed for the 2.07 MPa motor and was subsequently redesigned to improve motor performance and motor reliability. There are two notable differences between the designs. Firstly, a post-combustion chamber was added to promote mixing before exiting the nozzle. Secondly, an increased pre-combustion chamber was also added to encourage increased oxidizer vaporization prior to entering the fuel grain. Unfortunately, these additions required the L_{grain}/D_{grain} ratio to decrease to accommodate the added space. Grain dimensions for each test can be found in Table 3.

Table 3. Hybrid motor fuel grain dimensions.

Test #	P_C (MPa)	D_{grain} (mm)	L_{grain} (mm)	L_{grain}/D_{grain}	Pre Chamber (mm)	Post Chamber (mm)
1	2.07	33	396	12	45	N/A
2	4.83	58	580	10	70	25
3	3.45	50	500	10	120	50

2.6 Injector Design

Injectors are one of the largest contributors to combustion instabilities and require special consideration with regards hybrid motor design [27]-[31]. Injectors serve to atomize the liquid oxidizer and to promote mixing within the combustion chamber. Traditionally, conical spray patterns have been used in a wide range of applications from liquid rocket motors to internal combustion engines where oxidizer-fuel mixing throughout the entire vessel is encouraged. Conversely, wide spray cones in hybrid rocket motors have directly contributed to combustion instabilities due to the formation of recirculation zones at the front of the fuel grain, shown in

Figure 10 [27]-[31]. These vortices recirculate combustion gas upstream of the fuel grain and momentarily consume the oxidizer near the injector. This produces a combustion event where the sudden increase in pressure restricts the flow of oxidizer and causes the motor to become extremely fuel rich. This subsequently causes the flame to diminish, lowering the combustion chamber pressure. As such, the pressure gradient across the injector increases, causing oxidizer to flood the combustion chamber and return the motor to stoichiometric combustion. This influx of oxidizer, in conjunction with combustion gas recirculation, produces a second combustion event that causes the process to repeat itself. This particular instability is referred to as "chugging" and is extremely common in hybrid rocket motors [1], [28], [29].

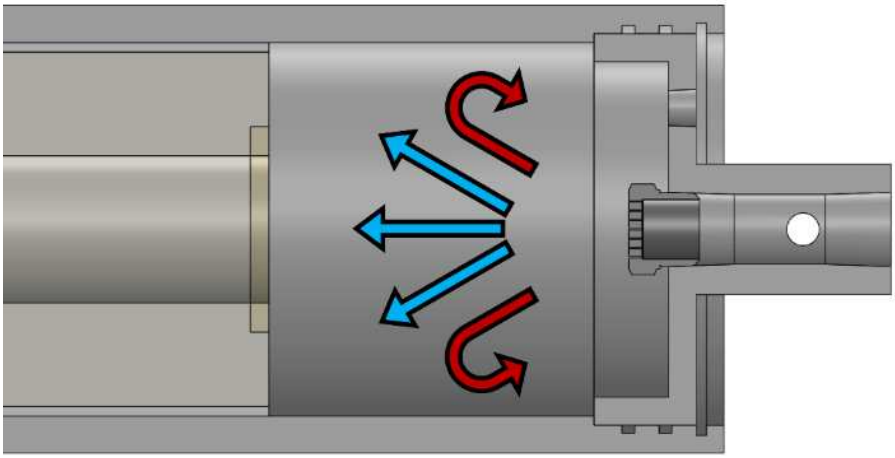

Figure 10. Representation of oxidizer recirculation within the precombustion chamber. Blue arrows correspond to the oxidizer flow and red arrows represent the unwanted recirculation of combustion gases.

One way to minimize recirculation instabilities is to use injectors that produce much tighter sprays to direct oxidizer into the grain and reduce the amount of oxidizer available to recirculate. Therefore, axial, or showerhead, injectors that produce strong axial streams have been shown to reduce instabilities [27]-[33]. Research also indicates that an impinging jet design promotes more vaporization compared to showerhead designs, while also maintaining the necessary center stream needed for efficient combustion [32]. Furthermore, designs with large pressure gradients across

the injector minimize boundary layer growth within the injector bores [34], [35]. This decreases the tendency for nitrous oxide to cavitate and choke the flow by reducing the amount of low pressure zones. The second benefit of high-pressure gradients is the reduction of pressure wave propagation traveling through the injector, like those experienced during chugging instabilities [33]. Previous research has shown that an injector length to diameter ratio (L_{port}/D_{port}) less than 10 reduces the potential for cavitation by limiting the boundary layer within the bore [34]. Note that the length to diameter ratio refenced here specifically refers to the injector port length and injector port diameter.

In summary, injectors that demonstrate strong axial streams, high atomization or vaporization, and steady flow characteristics were considered the most adventitious. Although N_2O will naturally vaporize within the motor, a slow rate of vaporization would cause a decrease in fuel regression at the front of the fuel grain, leading to an increase in the O/F ratio and decreased performance. Similarly, asymmetric spray cones or inconsistent flows suffer from many of the same issues associated with vaporization, wherein one side of the fuel grain preferentially burns creating inconsistencies within the flow that lower efficiency.

For those reasons, three showerhead type injectors and one impinging injector were tested. However, the impinging jet injector was subsequently abandoned for later testing due to manufacturing reasons. The showerhead injector consists of clustered straight bores rather than a singular port to minimize oxidizer particle size when leaving the injector. The impinging injector is designed with a series of 40° impinging jets that surround a traditional showerhead design (Figure 12). The mixed design was, in large part, a result of manufacturing limitations and size restrictions. The dimensions of the injectors can be found in Table 4 as well as photos of the injectors in Figure 11 and Figure 12. Note that throughout the testing process, each injector was

evaluated after each hot fire and adjusted accordingly. Hence the changes in the discharge coefficient and the number of ports between designs.

Table 4. Injector design parameters for each test case.

Test Case	ΔP_{inj} (MPa)	D_{port} (mm)	L_{Port} (mm)	L_{port}/D_{port}	C_d	# Ports	Type
1-a	2.76	0.94	3.18	3.38	0.7	12	Showerhead
1-b	2.76	0.53	1.91 - 3.10	3.60 – 5.85	0.7	44	Impinging
2	1.38	0.79	2.36	2.99	0.5	75	Showerhead
3	2.07	0.46	2.36	5.13	0.55	127	Showerhead

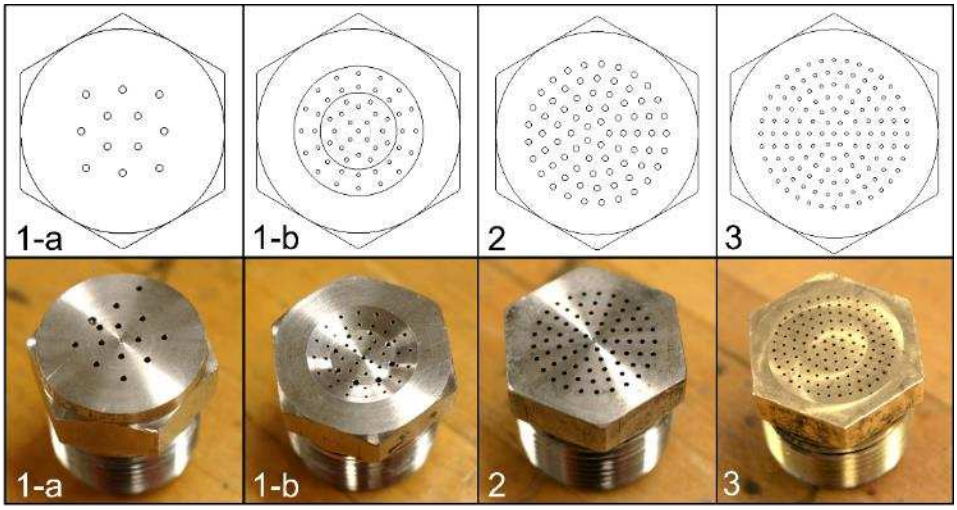

Figure 11. Images of designed and tested injectors where the top row are top-down drawings and bottom row are the associated photos. case 1-a and 1-b represent the showerhead and impinging jet designs respectively, and cases 2 and 3 are both showerhead designs.

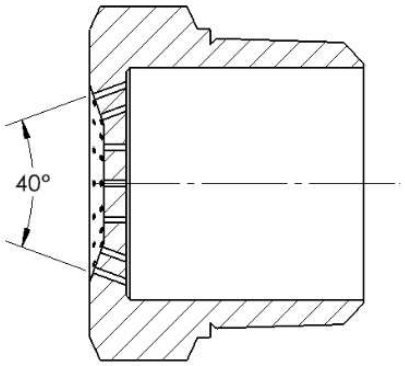

Figure 12. Cross-section view of the impinging jet injector (case 1-b) showing a 40° impingement angle.

CHAPTER 3 - EQUIPMENT AND INSTRUMENTATION

3.1 Hybrid Rocket Motor Thrust Stand

The primary equipment for this research centered around a mobile hybrid rocket motor thrust stand (HRMTS). The system was originally developed by Sierra Nevada Corporation and loaned to Colorado State University to provide a testing platform for the undergraduate Intercollegiate Rocket Engineering Competition team. The undergraduate team has since moved to a different motor type and therefore no longer needed the thrust stand. Since then, the equipment had fallen into a state of disrepair and required significant modifications and modernizations since its last use in 2016.

Currently the HRMTS is capable of measuring motor thrust up to a 5000 lbf fed by a central nitrous oxide tank with a maximum operating pressure of 1000 psi. The HRMTS consists of four sub-systems surrounding a central oxidizer tank (C): tank pressurization (A), oxidizer filling (B), motor purge (D), and motor test sled (E). Integration of the sub-systems are shown in Figure 13 and Figure 14. Letter designations refer to the corresponding sub-systems shown Figure 13 and Figure 14.

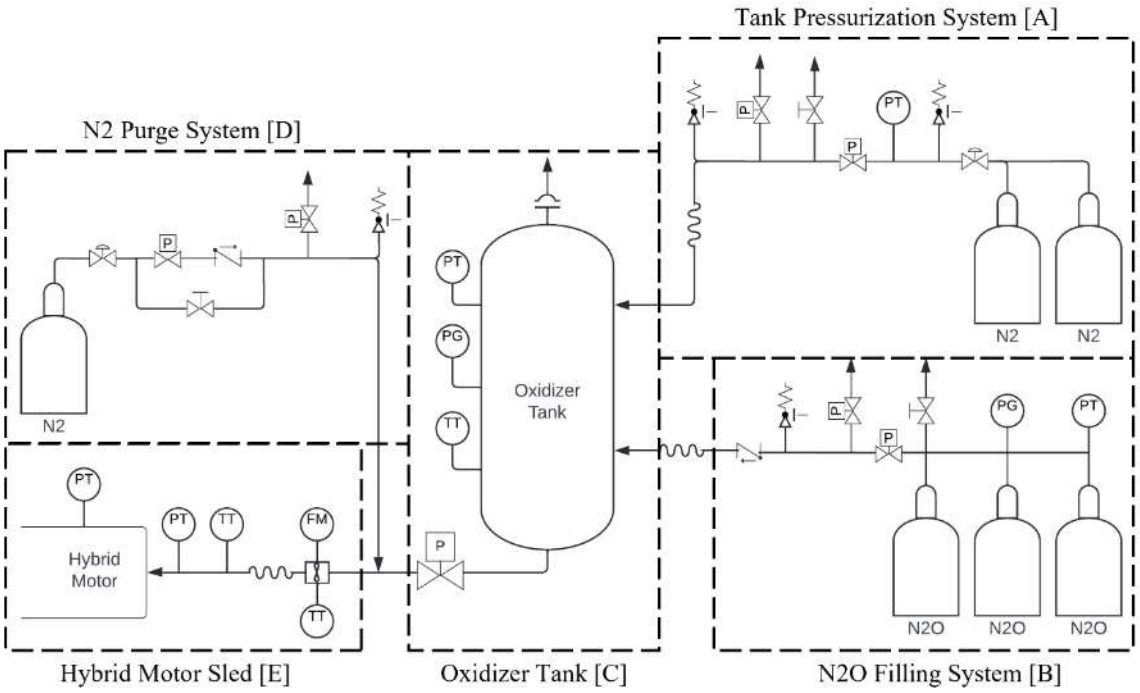

Figure 13. Piping and instrumentation diagram for the hybrid rocket motor test stand.

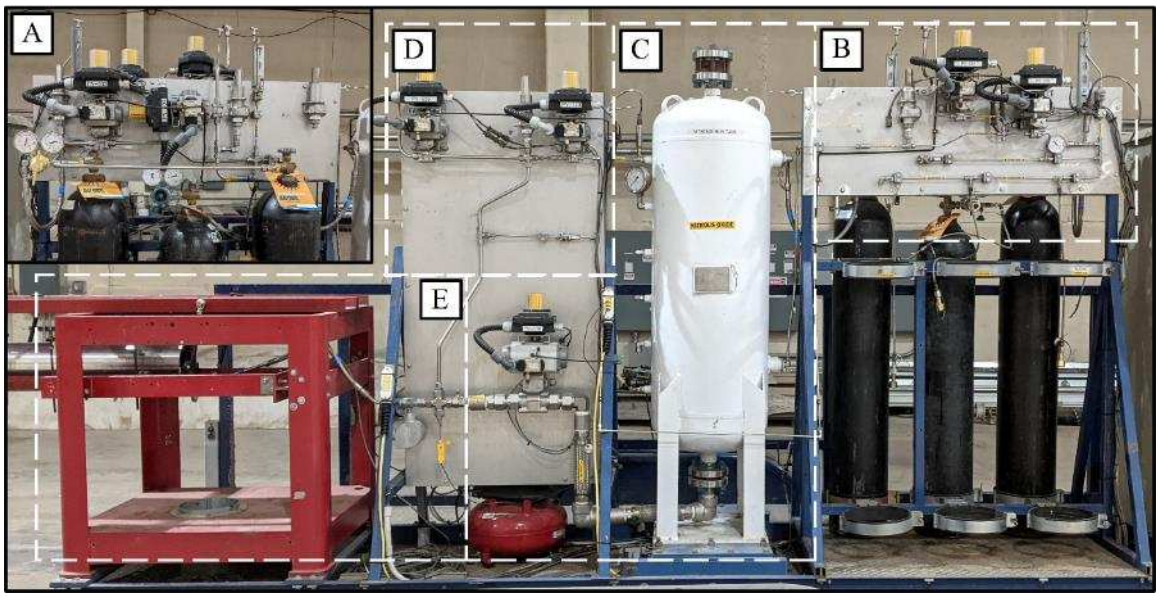

Figure 14. Photo of the hybrid rocket motor thrust stand.

During testing, the system first draws oxidizer from a primary oxidizer tank (C) to not be limited by flow restrictions like those found when drawing directly from N_2O gas cylinders. The oxidizer tank implements multiple thermocouples as well as a diaphragm pressure transducer and

pressure gauge to determine the thermodynamic properties of the oxidizer. One thermocouple measures the headspace temperature while the other measures the fluid temperature directly. Four 250 lbf beam load cells are affixed to the bottom of the tank to measure oxidizer mass during filling and discharge. The bottom of the tank leads to the primary pneumatic discharge valve that controls the flow of oxidizer to the motor. An additional 1.25 lpm turbine flow meter and associated thermocouple were added after the first test fire to improve oxidizer mass flow rate measurements.

The nitrous oxide filling sub-system (B) fills the primary oxidizer tank by drawing directly from three 200 ft^3 nitrous oxide cylinders equipped with syphons. An in-line pneumatic valve controls the flow of oxidizer to the tank. A secondary pneumatic valve, nested between a one-way poppet check valve, is used to clear the line of oxidizer after filling. Importantly, the one-way poppet valve separates the oxidizer tank from the filling system, which makes it possible to clear the lines of oxidizer and create a barrier between the tank and the gas cylinders.

The pressurization sub-system (A) uses two 300 ft^3 nitrogen gas cylinders, regulated by a high flow single stage regulator, to pressurize the tank after filling and for continual pressurization during motor operation. Pressurizing the oxidizer tank guarantees that the nitrous oxide will remain in a liquid state regardless of ambient temperatures and minimizes changes in mass flow rate due to changes in injector pressure. Similar to the nitrous oxide sub-system, a primary valve controls the flow of nitrogen to the tank, yet the secondary relief valve remains connected to the oxidizer tank and vents the entire tank after testing (or in case of an emergency). After the initial pressurization, the system activates during testing to maintain constant tank pressure by backfilling the tank with nitrogen.

Post-test fire, the oxidizer is vented from the feed line and nitrogen is forced through the oxidizer lines and hybrid motor by the motor purge sub-system (D). The main function of this system is to extinguish any lingering flames within the motor. Although the flames will likely suffocate, vaporized fuel may build up inside the motor and spontaneously combust if not addresses. The second function of the purge system is to clear any and all oxidizer from the feed lines. Without pressure forcing the oxidizer in one direction, there is a chance that the flame may propagate into the oxidizer lines causing catastrophic failure.

Throughout the thrust stand, 1000 psi spring actuated relief valves are scattered throughout each sub-system to ensure that no line exceeds the maximum operating pressure of 1000 psi. For the exact placements, refer to Figure 13. For redundancy, the oxidizer tank is fitted with a 1000 psi burst disk in case of motor failure or flame propagation into the oxidizer line. Furthermore, the tank pressurization (A), oxidizer filling (B), and post burn line purge (D), are equipped with pneumatic relief valves to vent line pressure remotely. To that end, manual ball valves, that vent to the atmosphere, have also been implemented to depressurize lines in case of power failure while the system is active or for added safety during storage.

Finally, the motor is suspended by a four-bar parallelogram sled that provides unimpeded axially movement while minimizing vertical and lateral motion. A load cell, capable of measuring 5000 lbf, is located at the rear of the sled to measure motor thrust. Three motor clamps secure the motor top to the sled and are modularly designed to accommodate multiple motor casing diameters. See Figure 15 labeling each of these parts.

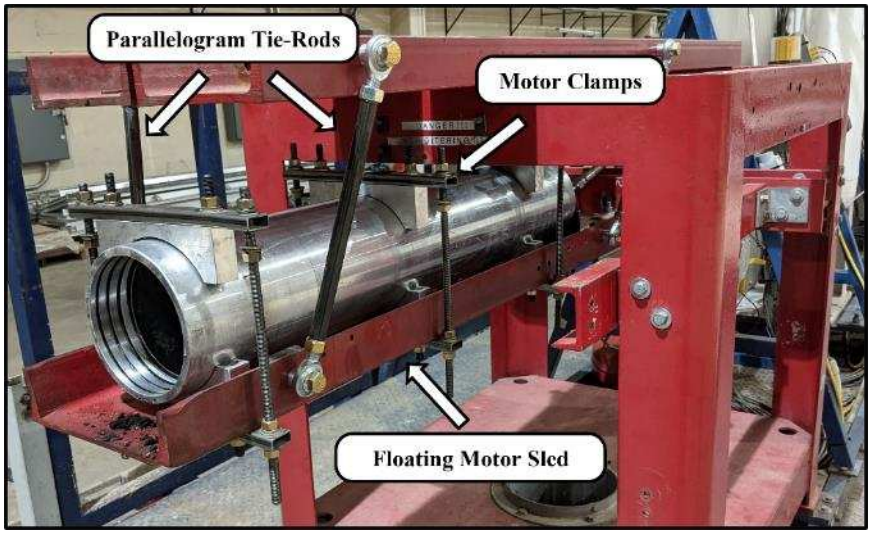

Figure 15. Photo of the sled assembly and combustion chamber.

3.2 Data Acquisition System

The thrust stand utilizes a National Instruments 9082 CompactRIO (CRIO) for data acquisition and mechanical operation. Since the CRIO is an integrated controller, where the LabVIEW VI runs independently of external hardware, many of the thrust stand operations have been automated. As such, the system is broken into four distinct operational loops: Input and output signals, data recording and GUI, front panel operation, and automated loops. The interaction between each system can be seen in Figure 16.

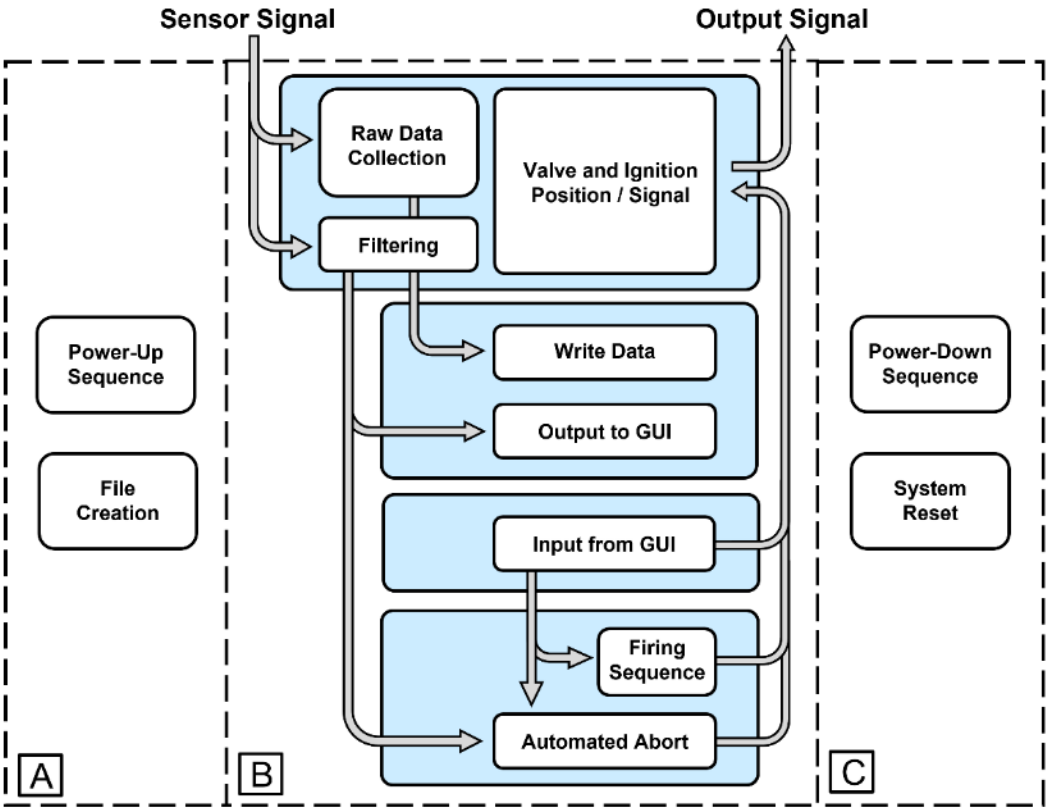

Figure 16. Back panel LabVIEW operation. Columns A, B, and C are the system startup, motor operation, and shutdown sequences respectively. The operational loops are shown in column B and divided into four grouped rows. Moving from top to bottom: signal/output, data logging, GUI input, and automated sequences.

The columns A and C in Figure 16 refer to the startup and shutdown routines performed to initialize sensors, file creation, and backup. Most of the processing and standard operation are contained within column B. Firstly, signal data is processed and filtered using a lowpass Butterworth filter before being sent to the second operational loop and recorded. This loop also processes output signals from the front panel GUI or the automated operational loops. After the raw and processed signal data are recorded, relevant signals are sent to the front panel and the automated abort loops. From the front panel, manual inputs are sent to either the firing sequence routine, abort routine, or output signal processing.

Each loop samples such that the systems with higher priority sample faster than the systems where expediency or critical operation is less important. Specifically, signal input and processing

sample at the highest frequency, 1 kHz, followed by the automated subroutines at 500 Hz, data logging at 100 Hz, and front panel at 50 Hz. This ensures that any gaps in time signatures or dropped data points do not affect lower subroutines. Note, LabVIEW is set up such that the previous data point is stored when data is dropped or interrupted. Collected data is divided and saved into three categories: filtered data, raw sensor signal, and front panel input logic and valve position. Data filtration utilizes a lowpass Butterworth filter before saving and display on the front panel. The raw signal data and logic are not displayed on the front panel but are still recorded for redundancy.

CHAPTER 4 - HOT-FIRE AND INJECTOR TEST RESULTS

This chapter discusses the test results from the preliminary injector tests in addition to the three hot-fire tests. Additionally, it addresses results and many of the nuances for each hot-fire test before discussing the erosion calculations found in the next chapter. Much of the testing was an iterative process and therefore informed future designs. For example, the injector tests were performed between test fires despite the data being presented at the same time. This is also true for the motor design, hence the small changes between test conditions.

Injector tests consisted of discharging nitrous oxide through each injector to the atmosphere until steady flow was visibly reached. Unfortunately, matching the pressure drop across the injector would result in a tank pressure lower than the saturation pressure, thus tests were carried out at the desired tank pressure associated with that test case. With that in mind, the gathered data was compared to an adjusted mass flow rate based on the measured ΔP_{inj}, injector temperature, and designed C_d instead of the mass flow rate required for the test fire. This means that the discharge coefficient does not produce a one-to-one comparison between motor operation and cold flow testing. Nevertheless, testing provides a basis for evaluating spray patterns and atomization as well as informing injector performance relative to the phenomena experienced during hot fires.

All hot-fire tests utilized the same pre-programed firing sequence. This started with a 1 second ignition signal, where resistive wire is heated to ignite the solid ignition grain, followed by a 3 second delay that allows for heat to build up within the motor and consumption of the ignition grain. At which point, the primary discharge valve is opened and remains open for 30 seconds. Motor operation is considered to last 30 seconds, since the valve is open for that duration. Nevertheless, a one second delay occurs between valve closure and full motor shut down. This delay can be seen in many of the figures displayed throughout this section. To that end, data

analysis does not include these transient events at the start and end of the test fire. Finally, the nitrogen purge lasts for 15 seconds but is often opened multiple times after the test fire to extinguish any reignited flames caused by the high internal temperature. Due to the differing oxidizer tank requirements, the oxidizer filling and initial pressurization are not automated but are manually performed prior to each test.

4.1 Pre-Test Fire Injector Test Results

All cases, except for case 2, resulted in lower than predicted discharge with cases 1-a and 1-b being the largest deviation. This discrepancy stems from the original approximation being based on research regarding liquid oxygen rather than nitrous oxide. However, the initial discharge coefficient was merely a starting point and could easily be adjusted by increasing the tank pressure or by adding more holes to the injector after testing. Subsequent injector designs used coefficients much closer to the coefficients measured from cases 1-a and 1-b. Results from testing as well as comparisons of the discharge coefficients and mass flow rates can be seen in Table 5. Furthermore, transient photo sets displaying the spray development for each test can be found in Figure 17 through Figure 20.

Table 5. Measured injector discharge coefficients.

Test Case	Average ΔP_{inj} (MPa)	Designed C_d	Measured C_d	Theoretical $\dot{m}$ (kg/s)	Measured $\dot{m}$ (kg/s)
1-a	3.96	0.7	0.39	0.51	0.29
1-b	3.91	0.7	0.39	0.61	0.34
2	4.17	0.5	0.57	1.80	1.86
3	5.52	0.55	0.36	1.12	0.73

Beginning with cases 1-a and 1-b, the 1-a injector exhibited a wide, inconsistent spray that reached steady state after 1 second. Conversely, injector 1-b exhibited a fully developed flow within 100ms that consisted of a more coherent center stream and higher atomization. Because

particle size was not directly measured, increased spray opacity was assumed to be the result of higher atomization. An additional characteristic of the 1-a injector was that the oxidizer remains in a partial vapor state for case 1-a until 250 ms before transitioning to a fully liquid state. As a result, case 1-b, the impinging jet, would be most advantageous for testing in large part to the stronger center spray and faster steady state response.

The differences in discharge coefficients, shown in Table 5, were resolved by adding 9 additional holes to the existing 1-b injector, resulting in a 53-hole injector and a new theoretical C_d of 0.5. At the time, it was assumed that the oxidizer flow would likely experience lower impedance during testing due to the lower ΔP_{inj}, and as such the C_d was adjusted to 0.5 rather than the measured 0.4. Later test fires confirm that the discharge coefficient is much closer to 0.55, hence the designed C_d of 0.5 and 0.55 for cases 2 and 3. Photos showing the transient response can be seen in Figure 17 and Figure 18.

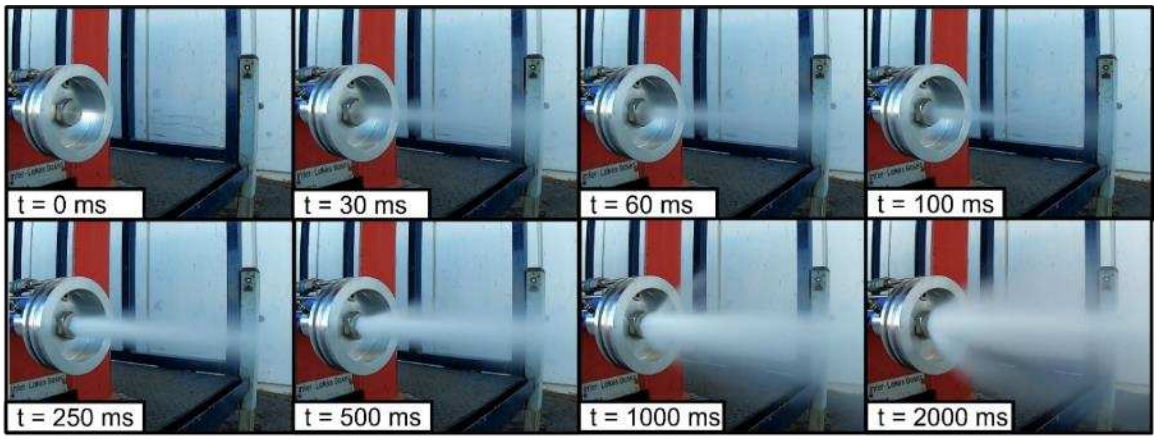

Figure 17. Case 1-a: Injector spray development over a period of 2000 ms, operating at an average ΔP_{inj} of 3.96 MPa.

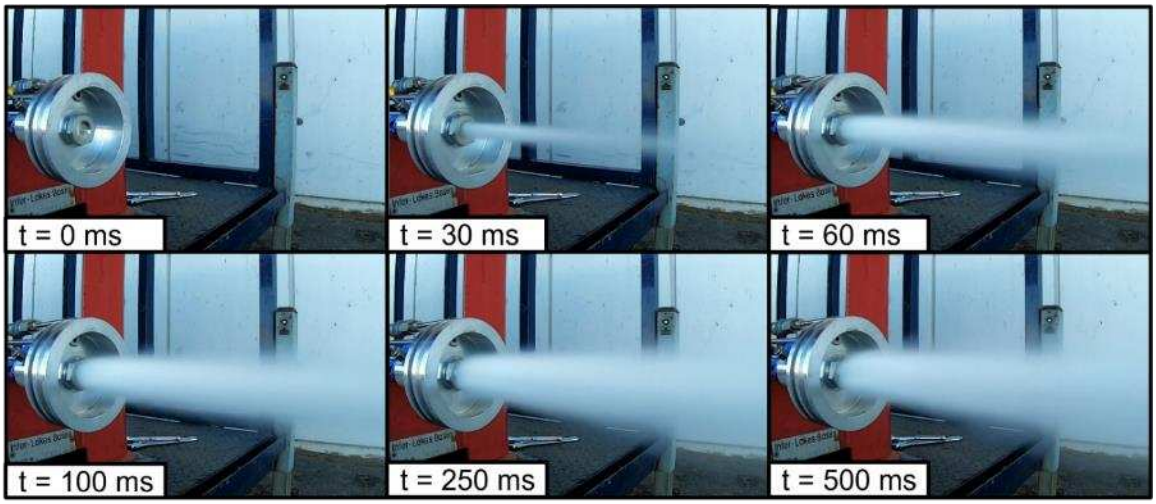

Figure 18. Case 1-b: Injector spray development over a period of 500 ms, operating at an average ΔP_{inj} of 3.91 MPa.

Injectors 2 and 3 were designed after the first hot-fire and iterated on the previous designs to improve combustion efficiency. Despite the poor performance from the previous showerhead injector, both cases 2 and 3 implemented showerhead designs due mainly to manufacturing limitations. The major improvement, though, was a reduced injector bore diameter aimed to decrease particle size. In theory, a smaller particle would vaporize more quickly, thus the emphasis on increased hole number and decreased port diameters. This rationale was taken one step further after the 4.83 MPa test fire, by nearly doubling the number of ports for the 3.45 MPa injector.

Cases 2 and 3 showed similar results to the impinging jet design, where both designs reach steady state at 100 ms and share many of the same spray characteristics as the 2.07 MPa impinging jet injector. Thus, the improved showerhead design was deemed suitable for hot fire testing. Notably, while testing injector 3, debris was found within the injector, which led to an artificially low C_d. The injector was still deemed suitable for testing based on the trends exhibited by the previous design. Figure 19 and Figure 20 show the development of the spray during the second set of cold flow tests.

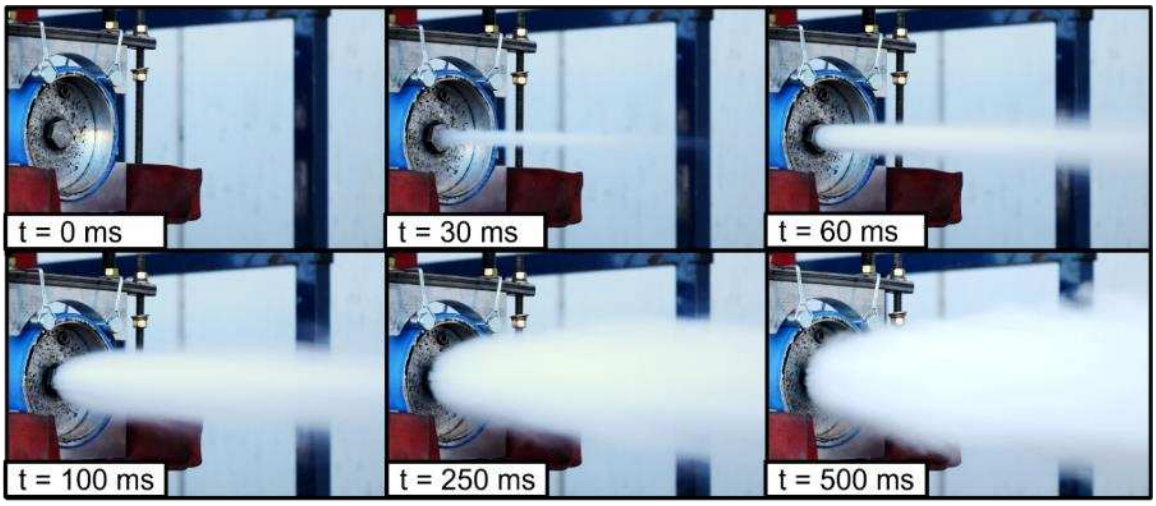

Figure 19. Case 2: Injector spray development over a period of 500 ms, operating at an average ΔP_{inj} of 4.17 MPa.

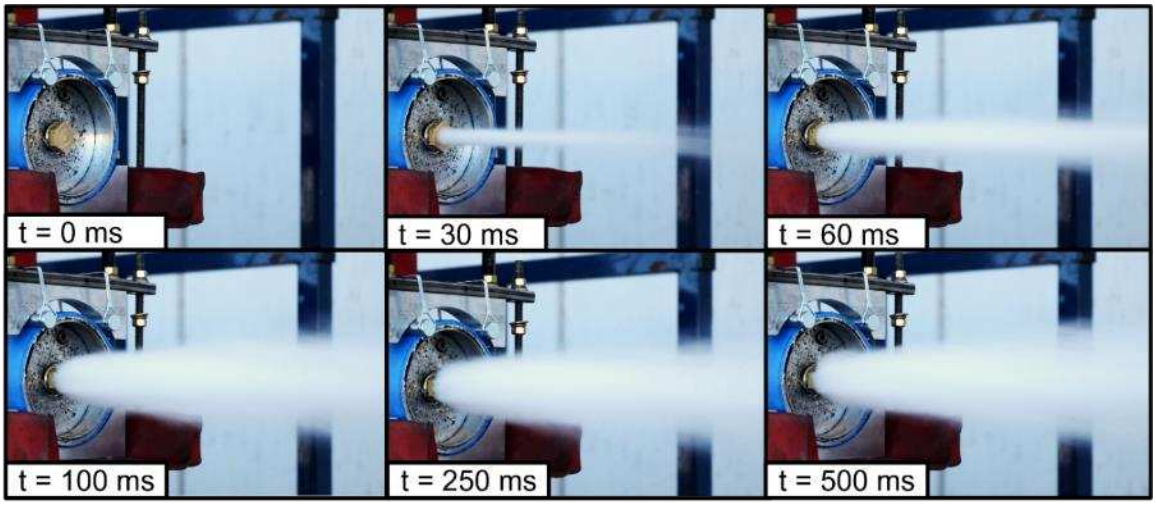

Figure 20. Case 3: Injector spray development over a period of 500 ms, operating at an average ΔP_{inj} of 5.52 MPa.

4.2 Test 1: 2.07 MPa Chamber Pressure

Figure 21. 2.07 MPa test fire.

The 2.07 MPa motor test resulted in an average thrust and chamber pressure of 0.91 kN and 1.53 MPa respectively, roughly 18% and 26% lower performance than expected. Figure 22 shows the thrust and pressure data from the test. Firstly, the motor experienced a hard start, wherein a detonation within the combustion chamber causes the chamber pressure spike when the oxidizer feed valve was first opened. Here, the hard start was a result of unburned solid fuel mixing with the oxidizer entering the motor, which momentarily increased the mass flow rate and increased the combustion chamber pressure. Figure 23 shows the flame caused by the detonation at motor start. Consequently, the pressure spike experienced in the first two seconds is not indicative of true motor operation and can be neglected during the analysis.

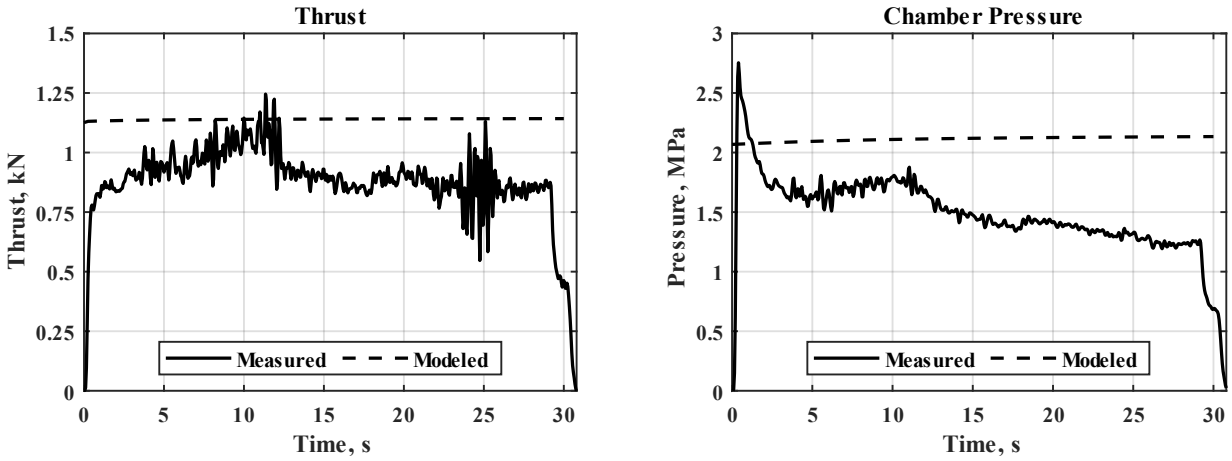

Figure 22. Thrust (right) and pressure (left) data from the 2.07 MPa test case. For both plots the dashed lines represent the expected modeled performance.

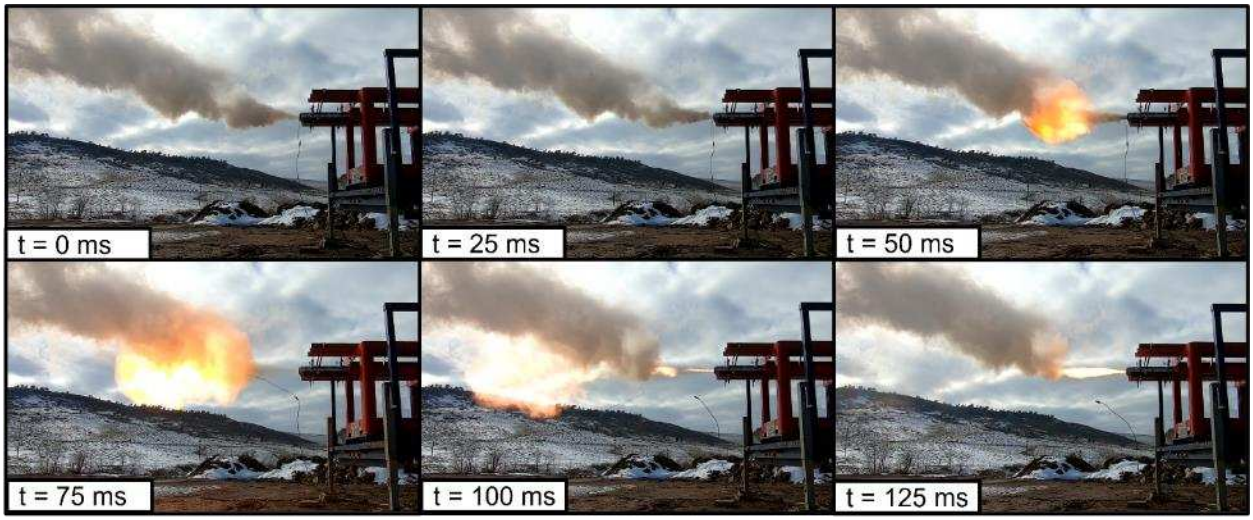

Figure 23. Photo set displaying the hard start detonation.

One of the most important features of the test, shown in Figure 22, is a point where the thrust and pressure transition from increasing to decreasing, approximately 12 seconds into the test. An increase in performance is to be expected because the motor is designed to reach peak performance midway through the test. On the other hand, the steady decrease in pressure does not align with expectations since it is not reflected in the preliminary modeling. The decrease in pressure and thrust is thought to be the result of motor erosion for two main reasons. Firstly, the

decrease in pressure remains relatively constant until motor shut off, which would indicate a constant erosion rate. Secondly, the thrust and pressure decrease simultaneously, which would occur when the throat area increases. Moreover, changes caused by mass flow rates can be ruled out because oxidizer flow remains unchanged throughout this is process (Figure 24).

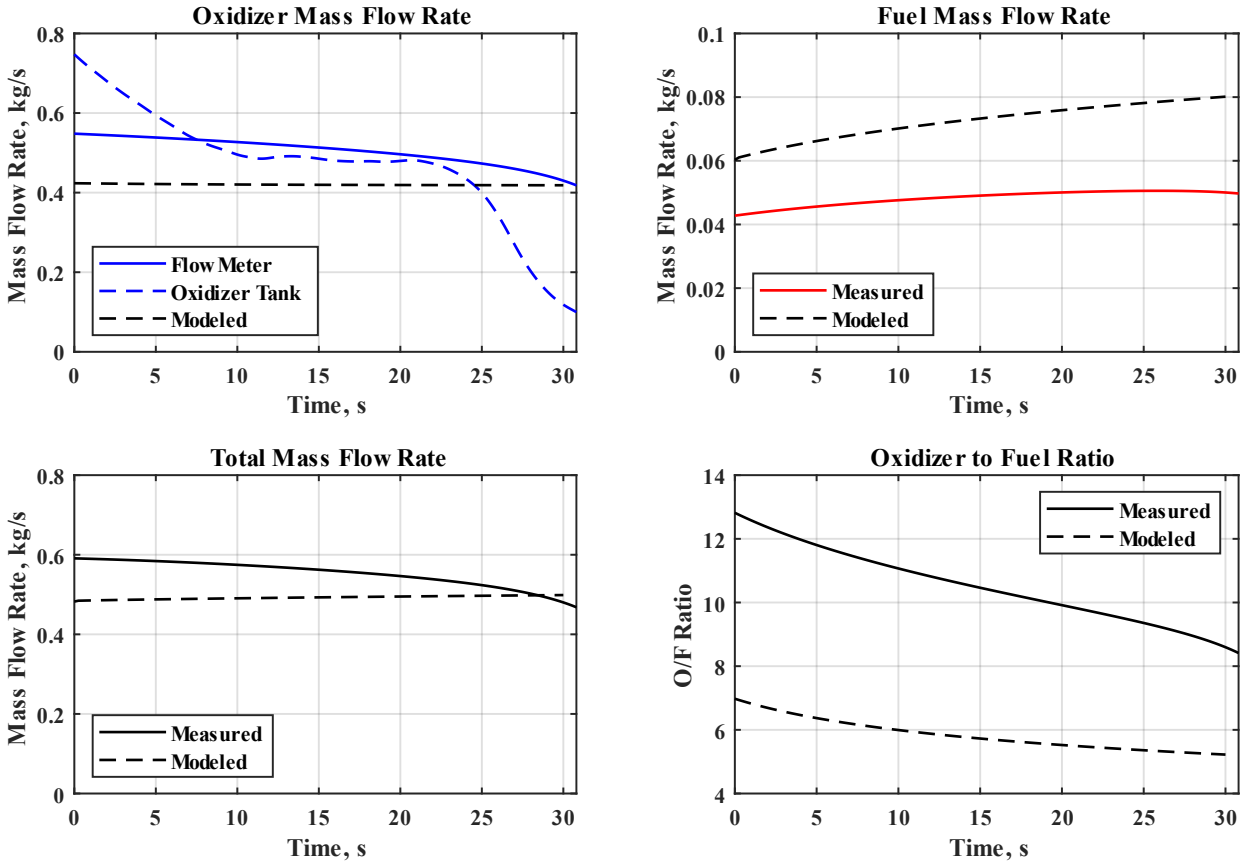

Figure 24. 2.07MPa: Plots showing the mass flow rate of the oxidizer (top left), fuel (top right), Total mass flow rate (bottom left), and the O/F ratio (bottom right). The oxidizer mass flow plot shows the flow rates gathered by the flow meter, the mass lost by the oxidizer tank, and the modeled mass flow rates.

Since the oxidizer mass flow rate is tied to the pressure gradient across the injector, the lower-than-expected chamber pressure caused flow rate to increase, thereby increasing the O/F ratio. This increase is further exacerbated by a lower-than-expected fuel mass flow rate. Despite the combined mass flow rate only being 12.3% higher than expected, the increased oxidizer mass flow rate in conjunction with the decreased fuel flow rate, the average O/F ratio spikes to 10.5,

nearly double that of the model. Table 6 documents the average differences in mass flow rates with Figure 24, showing the changes in mass flow rates and O/F ratio throughout the test.

Table 6. 2.07 MPa: Comparison of the average mass flow rates.

Propellant	Average Modeled $\dot{m}$ (kg/s)	Average Measured $\dot{m}$ (kg/s)	Difference (%)
Combined	0.49	0.55	+12.3
Oxidizer	0.42	0.51	+20.2
Fuel	0.07	0.05	-33.2

The increased O/F ratio causes the average C^* to lower from the desired 1620 m/s to 1000 m/s. Insufficient oxidizer diffusion, poor vaporization, or incomplete combustion could all contribute to the lower performance and poor combustion efficiency. One of the likely contributors is the low fuel grain regression and total mass loss resulting from inaccuracies in regression prediction. Subsequently, this would create a feedback loop that would further lower the combustion performance until a new steady state was reached. Additionally, the motor did not experience any notable combustion instabilities. This will become much more important and apparent for the 4.83 MPa and 3.45 MPa test.

4.3 Test 2: 4.83 MPa Chamber Pressure

Figure 25. 4.83 MPa test fire.

The 4.83 MPa test fire produced an average thrust of 1.70 kN and a chamber pressure of 2.73 MPa. Like the last test, the motor performed lower than expected with a decrease of 40.3% and 43.4% respectively. However, unlike the previous test, the factors that contributed to the decreased performance were much more tangible. Some of these factors include substantial combustion instabilities, insufficient pressure gradient across the injector, oxidizer changing phase prior to the injector, and inconsistent heating of the nozzle. Plots of the thrust and chamber pressure (Figure 26) demonstrate many of these features. Most notably, both thrust and pressure dramatically decrease after 18 seconds, which will be discussed in detail later, but the drop in performance is the result of nitrous oxide changing phase prior to the injector, not erosion. Additionally, data shows that the chamber pressure steadily decreases throughout the test, yet the thrust remains largely unaffected, making it a challenge to discern changes in performance caused by nozzle erosion.

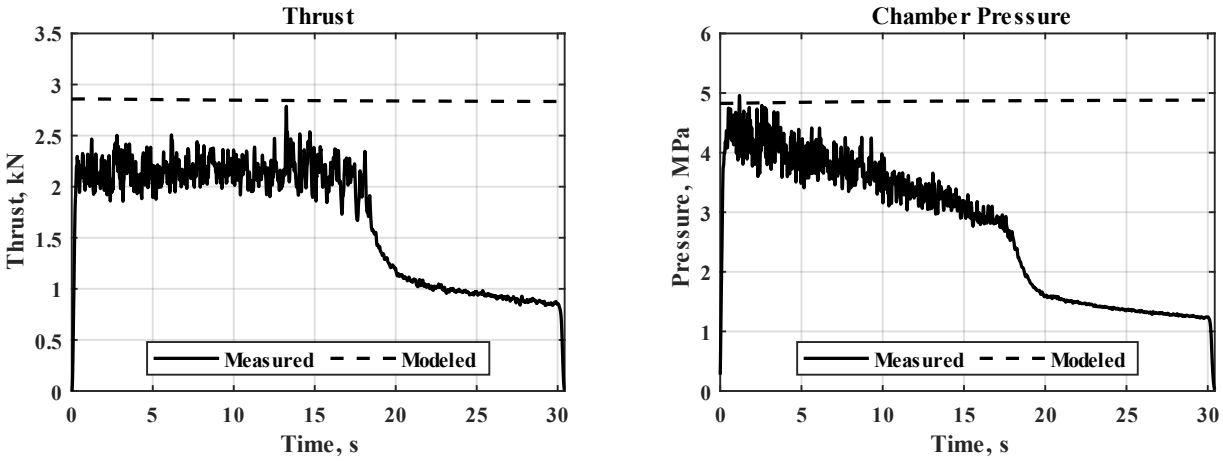

Figure 26. Thrust (right) and pressure (left) data from the 4.83 MPa test case. For both plots the dashed lines represent the expected modeled performance.

Firstly, the decreasing chamber pressure is tied to limitations within the nitrogen back pressurization system. Due to the high oxidizer mass flow rate needed for the test and the resulting rapid increase in the oxidizer tank headspace, the nitrogen back pressurization system was unable to maintain constant pressure. For the test, the oxidizer tank needed to be pressurized to 6.55 MPa to provide adequate pressure across the injector. Unfortunately, this consumed the entirety of the nitrogen cylinder and was never able to provide the necessary volumetric flow rate. In fact, across the entire test the tank pressure dropped a total of 1.7 MPa. Moreover, the maximum pressure reached inside the oxidizer tank was only 6.0 MPa, which led to issues at the injector. Furthermore, the presence of a one-way check valve upstream of the injector dropped the pressure an additional 1 MPa, resulting in an injector pressure just under 5 MPa. The injector was designed for a ΔP_{inj} of 1.38 MPa, meaning that the motor would never be able to reach the desired 4.83 MPa. Figure 27 compares the pressures within the oxidizer tank, injector, and combustion chamber.

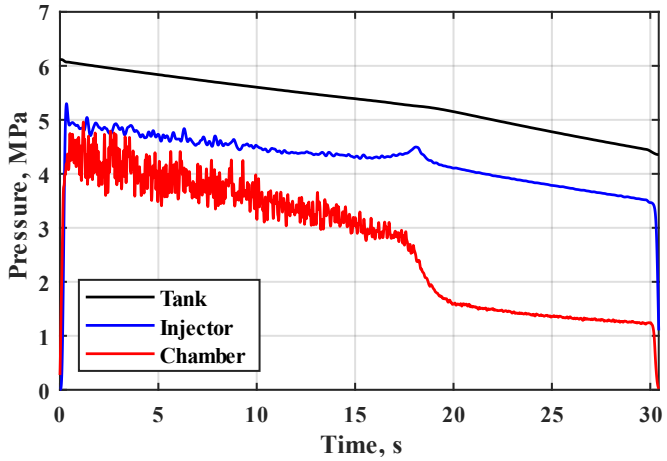

Figure 27. A comparison of the oxidizer line pressures for the 4.83 MPa test case.

Secondly, the insufficient pressure gradient across the injector created conditions where pressure waves could propagate through the injector. Although not the only contributor to combustion instabilities, pressure waves within the injector most certainly exacerbated combustion instabilities already present in the motor. These instabilities can be seen in Figure 26 and Figure 27, where the chamber pressure undergoes pressure spikes upwards of 1 MPa. Furthermore, pressure fluctuations within the injector can be seen in Figure 27, which is a perfect example of the cascading effect of combustion instabilities. Additionally, Figure 28 reveals the sputtering of the flame leaving the nozzle caused by the combustion instabilities. More about the instabilities will be discussed, but first it is important to address the phase change that occurs midway through the test.

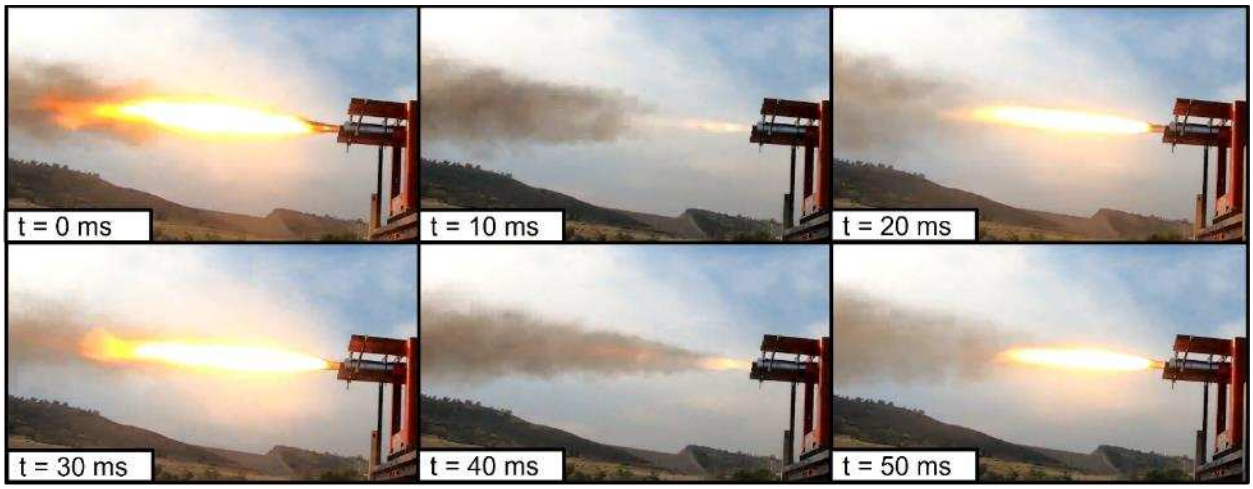

Figure 28. Photo set displaying the combustion instability seen in the motor flame.

Like Figure 24, Figure 29 shows the mass flow rates and O/F ratio during the 4.83 MPa test, as well as the density of the nitrous oxide. Immediately, several important features become apparent. 18 seconds after motor ignition, the density of the nitrous oxide drops from 900 kg/m^3 to roughly 120 kg/m^3, reducing the oxidizer mass flow rate from 1.12 kg/s to 0.13 kg/s - a reduction of nearly 700%. The differences in mass flow rates can be found in Table 7.

Table 7. 4.83 MPa: Comparison of average mass flow rates pre and post phase change.

Propellant	Modeled $\dot{m}$ (kg/s)	Pre-Phase Change $\dot{m}$ (kg/s)	Difference (%)	Post-Phase Change $\dot{m}$ (kg/s)	Difference (%)
Combined	1.12	1.27	+7.5	0.21	-81.2
Oxidizer	0.96	1.12	+15.8	0.13	-86.1
Fuel	0.16	0.15	-1.4	0.08	-54.0

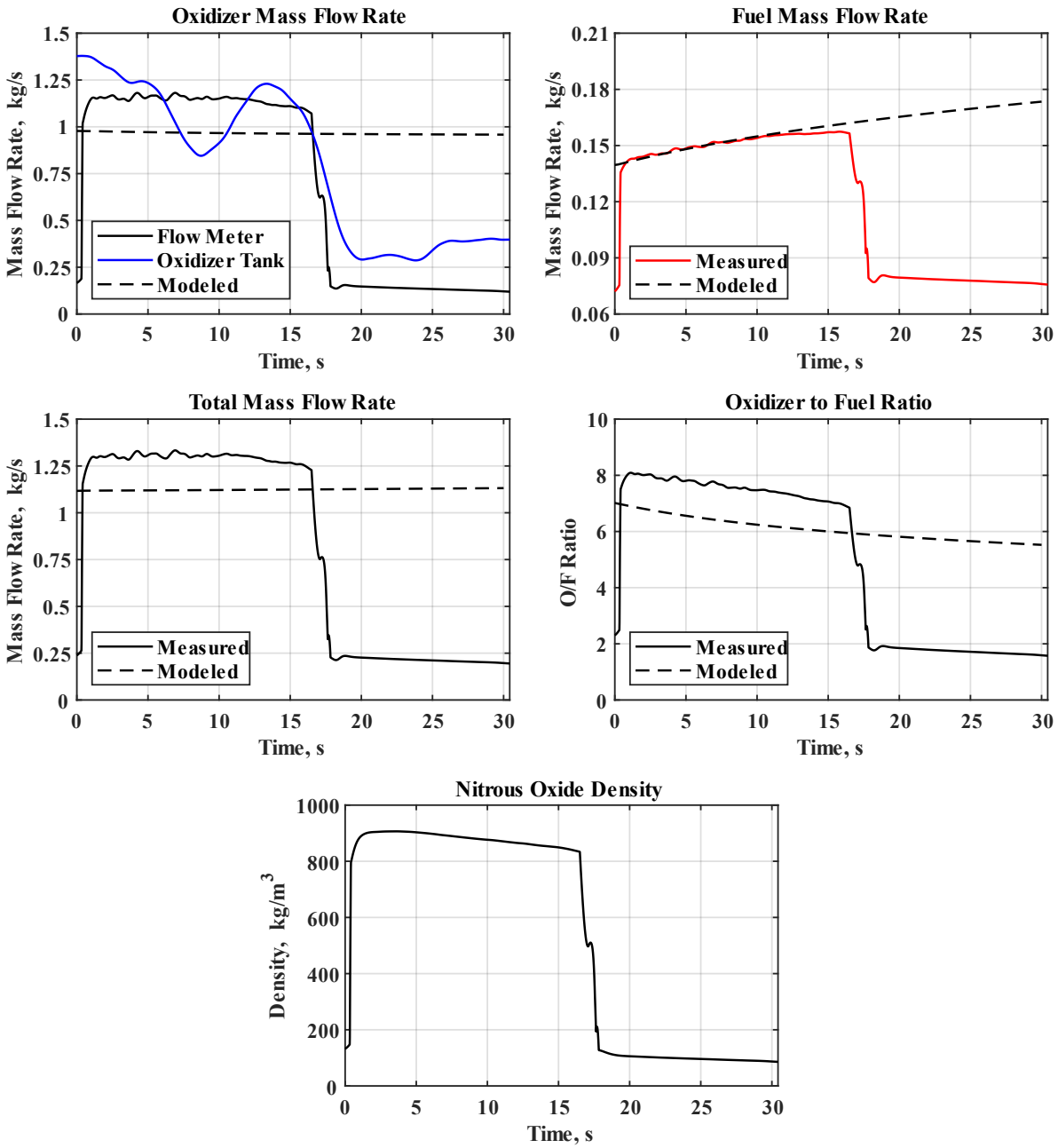

Figure 29. 4.83 MPa: Plots showing the mass flow rates, oxidizer to fuel ratio, and nitrous oxide density at the flow meter.

Because of the issues related to the oxidizer pressure, when the in-line pressure dropped below the saturation pressure, the nitrous oxide transitioned into a saturated vapor state. This caused the mass flow rate to decrease and subsequently reduce the combustion chamber pressure and thrust, hence the drop seen in Figure 26. Likewise, Figure 30 shows the normalized signal

gathered from the turbine flow meter specifically designed to measure liquids. As such, when the phase change occurs, gas starts passing through the flow meter, causing the turbine to spool up and max the signal output, further reenforcing the presence of phase change.

The transition to gaseous nitrous oxide causes a series of cascading effects. First off, fluctuations in the injector pressure subside. This is likely due to the increased pressure gradient resisting reversed flow. In turn, the combustion instabilities subside, though it is hard to discern if the instabilities were a result of poor mixing or poor oxidizer vaporization. Spectrograms found in Figure 31 show the decrease in pressure oscillations after the change in phase and the stabilization of the combustion.

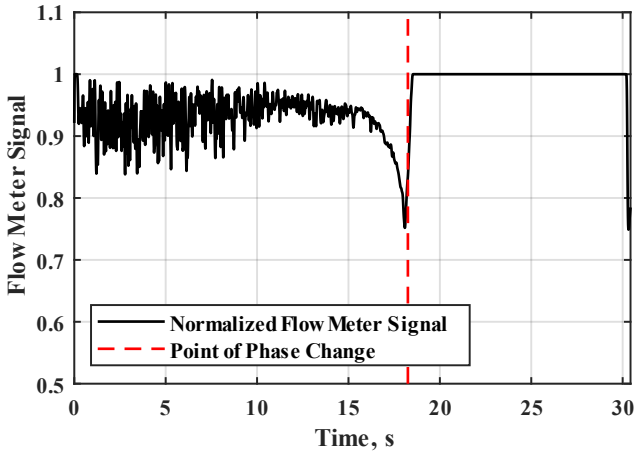

Figure 30. The normalized flow meter signal from the 4.83 MPa test with the dashed line indicating the point of phase change.

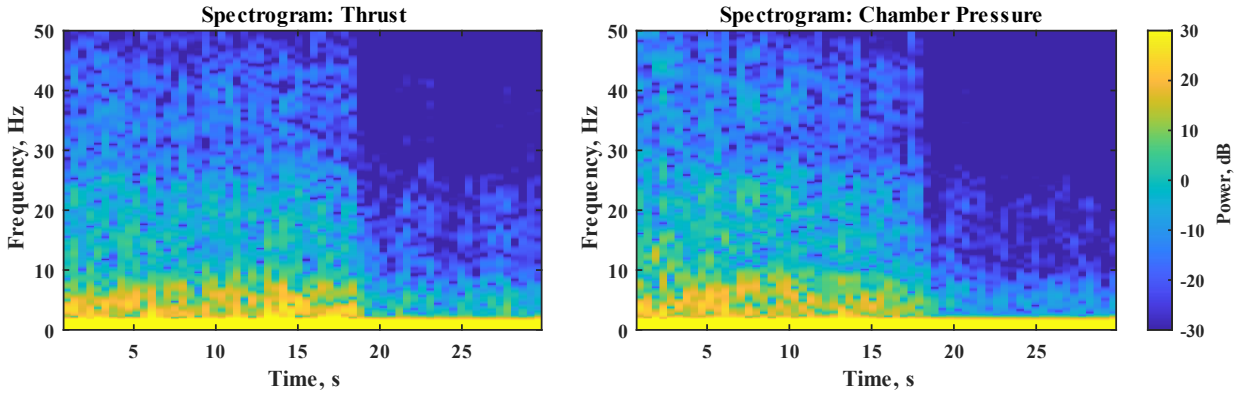

Figure 31. Spectrogram of the 4.83 Mpa test showing the transitant distribution of frequencies.

As a result of stable combustion, the temperature of the nozzle dramatically increases and the combustion exhaust becomes noticeably cleaner. Although these last two considerations are evaluated wholistically, they inform some of the interactions occurring at the nozzle. Figure 32 shows the change in flame characteristics pre and post phase change and the difference in soot present in the exhaust products. Despite being oxidizer rich, the exhaust products have more soot formation, suggesting incomplete fuel rich combustion, pre phase change. Conversely, the flame post phase change has little signs of sooting, implying stoichiometric or oxidizer rich combustion despite operating fuel rich. The O/F ratio pre and post phase change can be seen in Figure 29.

Figure 32. 4.83 MPa: Flame pre (left) and post (right) phase change.

The other side effect of stable combustion was the increase in nozzle temperature. Seconds after the phase change and the stabilization of the combustion, the nozzle begins to glow red, which is indicative of rapidly increasing temperature (Figure 33). Discussed earlier, the rate of erosion is

tied to the surface temperature of the graphite, whereby increased temperature leads to a lower activation energy and thus more erosion. As such, the increased nozzle temperature implies higher erosion despite the lower chamber pressure. This becomes extremely important for predicting erosion rates and will be discussed more in the next chapter.

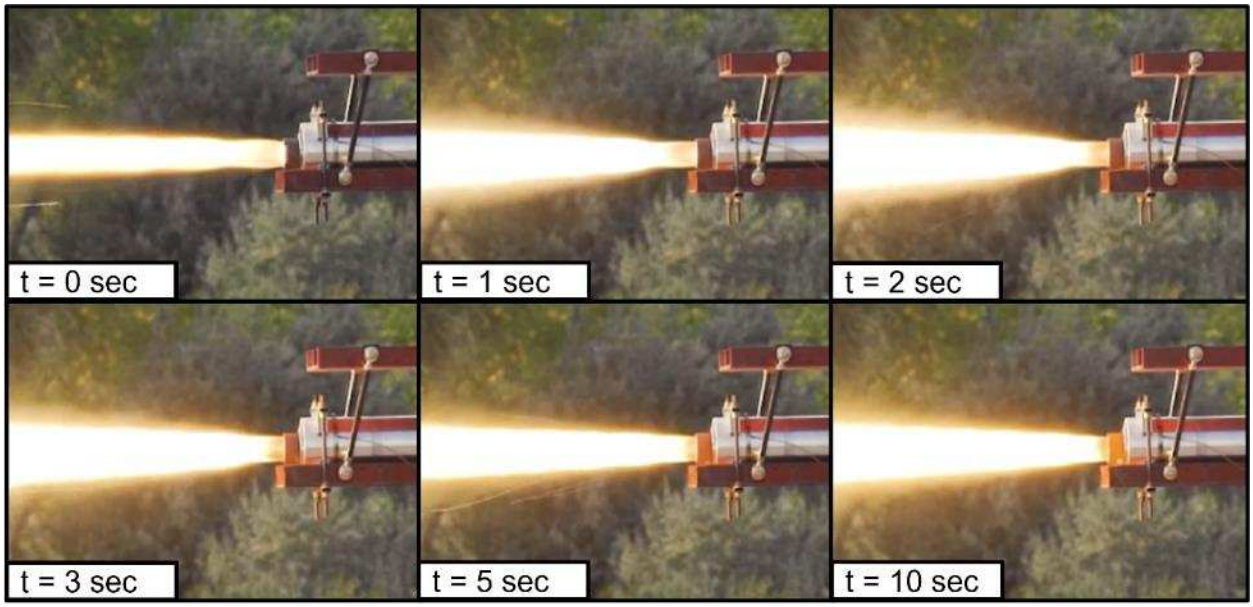

Figure 33. Photo set showing nozzle heating after nitrous oxide phase change. Here t = 0 represents the point of phase change, 18 seconds into the test fire.

4.4 Test 3: 3.45 MPa Chamber Pressure

Figure 34. 3.45 MPa test fire.

The 3.45 MPa test, much like the others, resulted in lower-than-expected performance with roughly 40% lower thrust and 30% lower chamber pressure at 1.37 kN and 2.07 MPa respectively. This test also closely resembles the previous case for which the thrust and pressure drop considerably after 12 seconds as well as combustion instabilities prior to the drop and subsiding after the drop (Figure 35). Furthermore, the same change in flame profile, displayed in Figure 36, also occurred at the 12 second mark. This is all to say, the 3.45 MPa test mimics many of the phenomena experienced in the previous 4.83 MPa test and suggests that the same oxidizer phase change occurred during this test. As such, many of the same assumptions discussed above can also be applied to this test. Nonetheless, the oxidizer mass flow rate and density do not have the same distinct decrease as seen in the 4.83 MPa test.

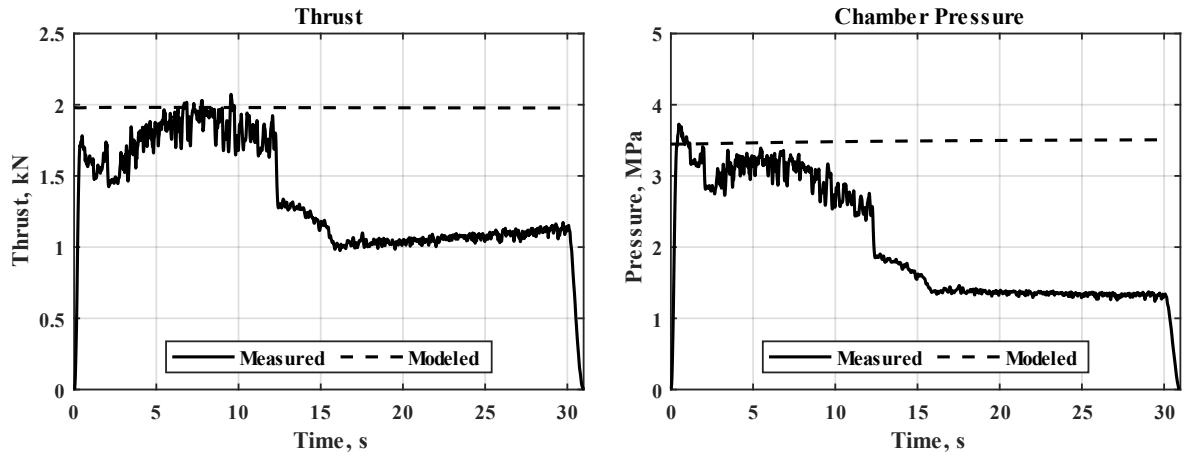

Figure 35. 3.45 MPa test case: Recorded thrust (right) and pressure (left) data.

Figure 36. 3.45 MPa: Flame pre (left) and post (right) phase change.

Since many of the same behaviors were measured between the 3.45 MPa and 4.83 MPa tests, it is highly likely that phase change occurred despite not measuring the same decrease in mass flow rate. Figure 37 shows the measured mass flow rates throughout the test where the oxidizer mass flow rate remains consistent across the entire test. Although, the oxidizer mass flow rate does decrease by 25% and can be partially attributed to decreasing tank pressure. A breakdown of the changes in mass flow rates can be found in Table 8.

Nevertheless, the change in flame profile and drop in performance are clear indicators of previously documented phase change. This may be the result of cavitation within the rear bulkhead

caused by instrumentation obstructing the flow and creating turbulence that lowers the pressure below the saturation pressure. Or cavitation may have occurred within the injector port due to the higher L_{port}/D_{port} ratio compared to the other injectors.

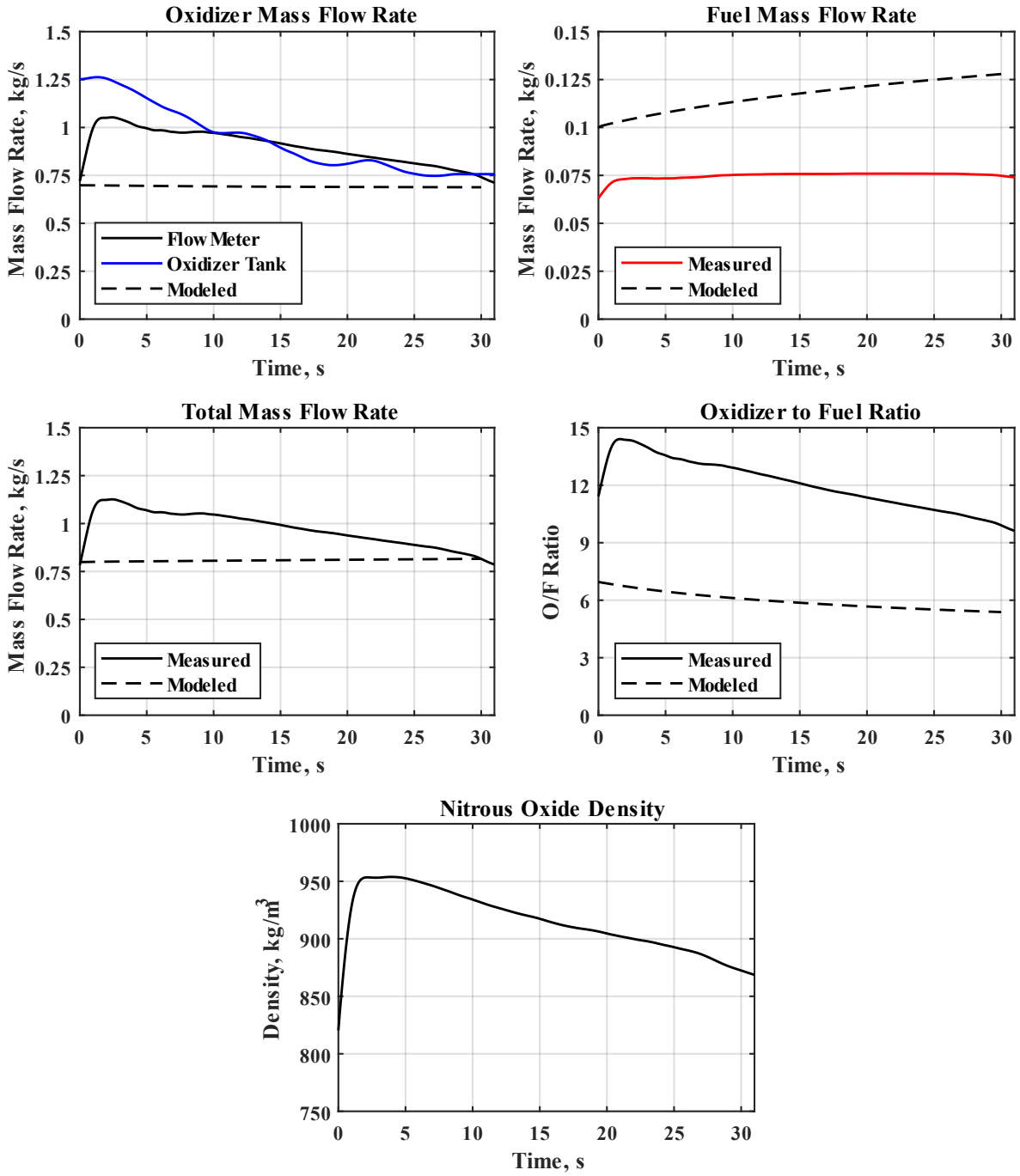

Figure 37. 3.45 MPa: Plots showing the mass flow rates, oxidizer to fuel ratio, and nitrous oxide density at the flow meter.

Table 8. 3.45 MPa: Comparison of average mass flow rates pre and post phase change.

Propellant	Modeled $\dot{m}$ (kg/s)	Pre-Phase Change $\dot{m}$ (kg/s)	Difference (%)	Post-Phase Change $\dot{m}$ (kg/s)	Difference (%)
Combined	0.81	1.06	+30.7	0.90	+1.4
Oxidizer	0.69	0.98	+41.5	0.82	+19.7
Fuel	0.12	0.07	-32.4	0.08	-38.7

In addition to phase change, similar combustion instabilities were present, including upstream injector pressure fluctuations and subsequent combustion stabilization post phase change, albeit much less severe. Like Figure 27, Figure 38, shows the oxidizer line pressures wherein fluctuations in injector pressure can be seen between 1.5 and 10 seconds. Unlike the previous test, the greater pressure gradient substantially reduced the magnitude of the fluctuation. This likely lowered the potential for combustion instabilities, indicating that the problem exists further downstream. Again, a spectrogram (Figure 39) shows the same phenomenon seen in Figure 31 and the notable decrease in high frequency oscillations after 12 seconds associated with combustion instabilities. This all gives further credence to the assumption that phase change is present during this test.

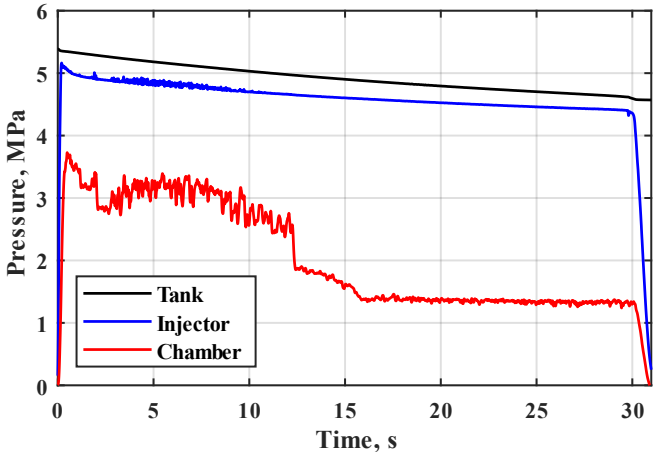

Figure 38. A comparison of the oxidizer line pressures for the 3.45 MPa test case.

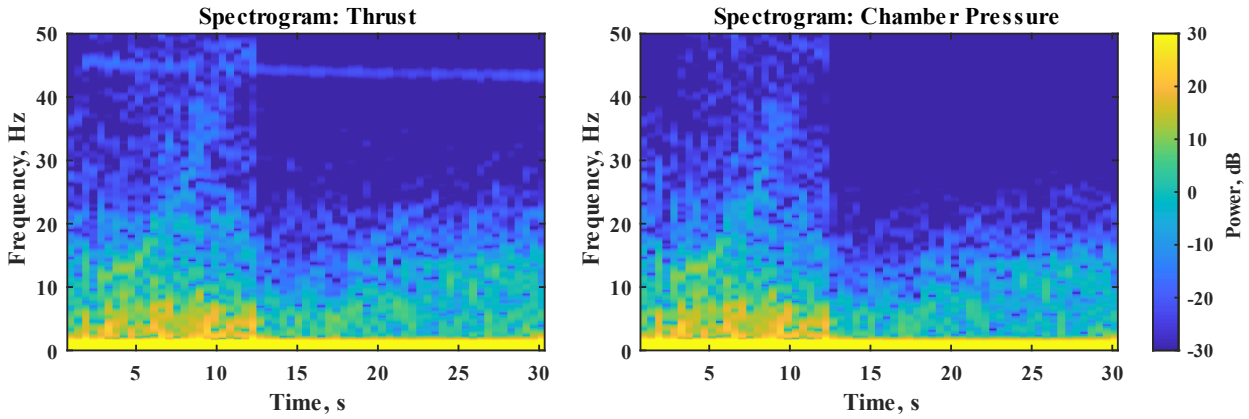

Figure 39. Spectrogram of the 3.45 MPa test showing the transient distribution of frequencies.

4.5 Hybrid Motor Test Summary

Now that the individual components of each test fire have been described, reoccurring findings and the major conclusions can be addressed. The clearest point of interest is the reduced performance across all tests. To reiterate, the 2.07 MPa test resulted in a 25% lower chamber pressure and the 4.83 MPa and 3.45 MPa tests resulted in a 40% decrease, approximately. Consequently, the oxidizer mass flow rate increased for all tests thereby increasing the O/F ratio. This becomes relevant when discussing erosion since increased oxidizer flow leads to increased oxidizing species and thus increased erosion.

In a similar vein, the increased nozzle temperature seen in the 4.83 MPa test was unfortunately not captured for the 2.07 MPa and 3.45 MPa tests due to limitations in camera equipment. Nonetheless, heating effects do need to be taken into consideration, especially when combustion instabilities are significant for nozzle temperature, demonstrated in the 4.83 MPa test. To that end, it is likely that the 3.45 MPa nozzle experienced the same increase in temperature thereupon increasing erosion. It is for this reason that the 4.83 MPa and 3.45 MPa tests are not

likely to result in meaningful data. That said, the 2.07 MPa test exhibited characteristics indicative of erosion with a clear point at which the performance decreases. Which makes the 2.07 MPa test an ideal for erosion calculations and is therefore the focus for the majority of the erosion analysis in the later chapter.

CHAPTER 5 - ADDITIONAL COMMENTS

Now that the individual components of each test fire are understood, some topics can be examined before discussing the final erosion analysis. Here the interaction between the fuel grain and the injector, as well as some final thoughts about combustion instabilities will be discussed. The chapter will conclude with the inherent uncertainties related to the fuel mass flow rate and the cascading effects it has on the analysis.

5.1 Injector and Fuel Grain

One way to infer injector performance and spray characteristics is the resulting profile of the fuel grain. Cross-sectional profiles where the fuel grain disproportionally regresses in one area, or widens, demonstrate inefficient or incomplete combustion. For example, less regression towards the injector indicates insufficient oxidizer vaporization at the injector, ergo poor oxidizer diffusion at the front of the fuel grain. Conversely, less regression near the nozzle indicates insufficient oxidizer delivery to the end of the fuel grain. Figure 40 shows the fuel grain cross-section after each of the test fires. Note that the change in thickness is critical for understanding spray profiles, not the wall thickness of the grain.

Firstly, both the 2.07 MPa and 4.83 MPa fuel grains show less regression toward the injector, signifying poor injector vaporization. Note that the 4.83 MPa and 3.45 MPa grains share the same outer diameter of 125 mm whereas the 2.07 MPa grain has an outer diameter of 100 mm. Interestingly, the change in wall thickness seen on the 2.07 MPa grain may be proportionally larger than the 4.83 MPa grain, but the slopes terminate at the same distance from the injector, roughly 225 mm. It is challenging to say whether this is linked to the droplet diameter, and by extension the injector port diameter, or a stream that does not break apart and overpowers the diffusion to

the grain surface. In contrast, the 3.45 MPa grain shows no signs of curvature with constant wall thickness throughout, suggesting sufficient oxidizer vaporization while also delivering adequate oxidizer to the end of the fuel grain. This may imply that the 3.45 MPa injector, or injectors with decreased port diameters, can outperform other larger straight bore injectors.

Finally, Table 9 contains a comparison between the measured discharge coefficients with the design coefficients, including the liquid and post phase change vapor coefficients. Testing shows that the 4.83 MPa and 3.45 MPa injectors outperformed the original design coefficients and operate closer to 0.7. Whereas the 2.07 MPa injector had a much lower discharge coefficient of 0.55. Because of the acute angles of the outer ports, the impinging jet design likely restricted the flow more than the straight bore designs, hence the decreased discharge coefficient.

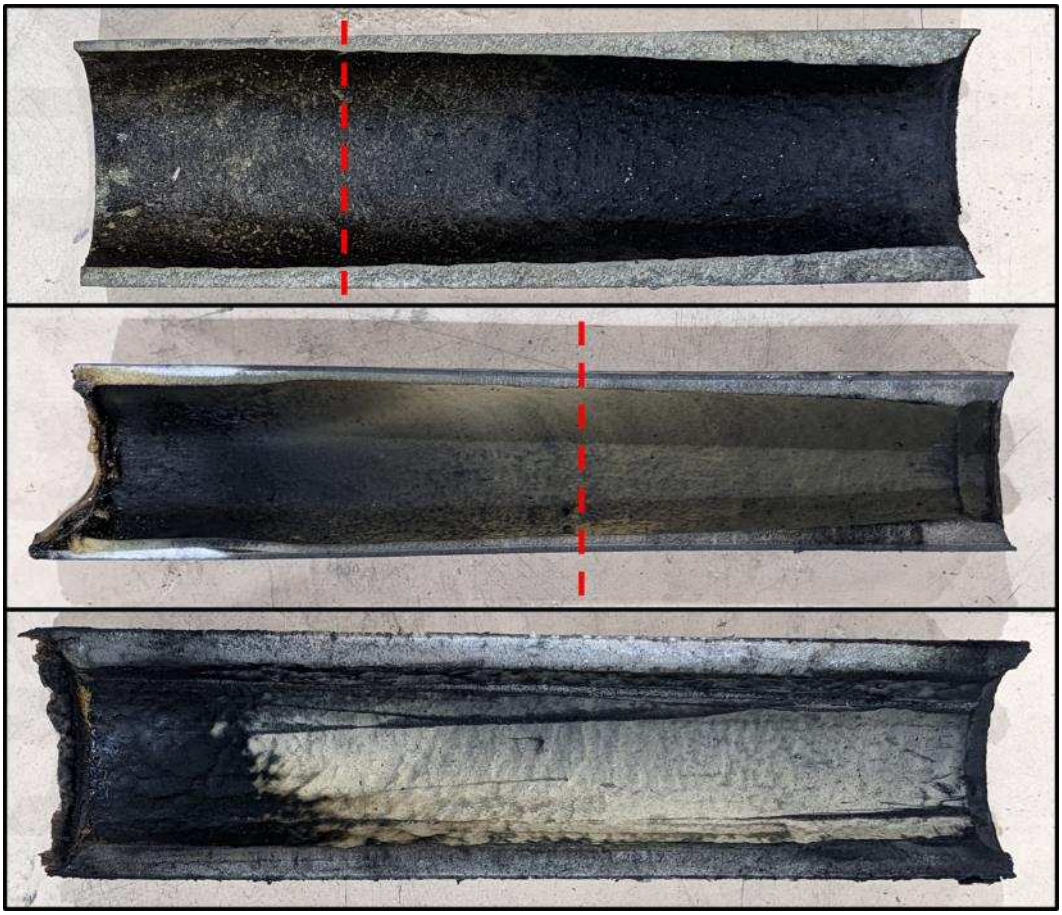

Figure 40. Spent fuel grains from each of the test fires. Starting at the top row and working down are the 2.07 MPa, 4.83 MPa and 3.45 MPa fuel grains. The dashed lines denote where the fuel grain wall thickness remains constant. The right side of the grain faces the injector, and the left side faces the nozzle. Ergo, combustion gases move from right to left.

Table 9. Comparison of designed and measured injector discharge coefficients.

Test Case	Designed C_d	Liquid C_d	Post-Phase Change C_d	Liquid ΔP_{inj} (MPa)	Post-Phase Change ΔP_{inj} (MPa)
2.07	0.45	0.55	N/A	2.63	N/A
4.83	0.50	0.77	0.17	0.87	2.42
3.45	0.55	0.77	0.50	1.81	3.14

5.2 Instabilities

Discussed previously, the causes of the instabilities may not be a direct result of poor injector design or a lack of upstream pressure. Rather, research suggests that vortex shedding and flow recirculation behind the fuel grain can induce combustion instabilities. Vortices are formed as combustion gases detach from the end fuel grain, creating a recirculation zone that induces instabilities, which are similar to the instabilities caused by poor injector design [26]. This means that if combustion instabilities were present as the fuel grain regresses, the instabilities would naturally subside as the recirculation zone decreases. Unfortunately, the phase change midway through the second and third test make it challenging to discern if vortex shedding is the cause of the instabilities, making it unrealistic to attribute the instabilities solely based on injector design without considering other aspects of the motor. Regardless, vaporization remains the likely culprit. In the 4.83 MPa and 3.45 MPa tests, the combustion post-phase change, where the nitrous oxide is presumed to be vaporized prior to the injector, is substantially more stable than any of the tests. This leads to cleaner combustion and presumably higher flame temperatures. More research is needed before more substantiated claims can be made.

5.3 Fuel Mass Flow Rate Predictions

Critically, the modeling conducted throughout this project relies on the O/F ratio to calculate thermodynamic properties. The major assumption used throughout this research assumes that the fuel mass flow rate can be accurately predicted. Nonetheless, the regression rate is empirically approximated and highly dependent on motor conditions. As such, the coefficients a and n from Equation 11, can fluctuate significantly. Ideally, regression rates would be found before testing but logistically this is not practical. For that reason, the regression rate and fuel mass flow

rate were adjusted during the analysis based on the differences in measured fuel grain mass loss and final grain diameter. Table 10 and

Table 11 list the differences in the modeled versus measured fuel grain mass loss and final port diameter, respectively. The tables also detail the adjustment coefficients applied to the fuel mass flow rate and regression rate during analysis. The coefficients were applied such that the calculated losses, based on the measured chamber pressures and oxidizer flow rates, would align with measured post-test fire fuel grain.

When compared to the model, both the measured mass loss and total fuel grain regression were lower than the predicted values for all tests. Back-calculations involving tests where combustion instabilities were present resulted in mass loss dramatically less than originally predicted. In contrast, calculations for the 2.07 MPa test, where instabilities were not present, were greater than the modeled mass loss and much greater than the measured loss. Unfortunately, comparisons between tests show no discernable patterns and as such the model used for back-calculations was only validated with two data points, pre-test fire and post-test fire. The other challenge, that becomes more apparent in the next chapter, is the changes in combustion resulting from the phase change midway through the latter two tests. This is all to say, that much of the analysis, especially related to the oxidizing species, is likely not indicative of actual conditions.

Table 10. Measured versus calculated fuel grain mass loss and adjustment coefficients for each test.

Test Case	Modeled Δm_{fuel} (kg)	Measured Δm_{fuel} (kg)	Back Calculated Δm_{fuel} (kg)	$\dot{m}_{fuel}$ Adjustment Coefficient
2.07	2.24	1.45	2.46	0.9
4.83	4.92	3.60	2.79	1.3
3.45	3.60	2.30	1.72	1.35

Table 11. Measured versus calculated total grain regression and adjustment coefficients for each test.

Test Case	Modeled ΔD_{grain} (mm)	Measured ΔD_{grain} (mm)	Back Calculated ΔD_{grain} (mm)	$\dot{r}$ Adjustment Coefficient
2.07	97.6	85.7	101.8	0.7
4.83	122.9	100.3	113.6	0.72
3.45	111.9	86.4	118.1	0.45

CHAPTER 6 - NOZZLE EROSION

Finally, the predictive model constructed in Chapter 2 was modified so the measured data could be implemented to back-calculate the motor properties, such as C^* and C_F. Nozzle erosion prediction and analysis largely focused on the erosion experienced in the 2.07 MPa test since the irregularities experienced in the 4.83 MPa and 3.45 MPa tests make it challenging to predict erosion. Nonetheless, an analysis of the 4.83 MPa and 3.45 MPa tests was conducted, which confirms many of the concerns expressed previously. Moreover, additional factors, such as oxidizing species and burn profiles were also taken into consideration throughout this process.

6.1 Nozzle Erosion Calculation and Assumptions

As a reminder, the characteristic velocity and the thrust coefficient are initially defined by measurable motor properties and as such the area of the throat, and subsequent throat diameter, can be calculated based on the theoretical values of C^* and C_F, determined by the O/F ratio. Therefore, erosion can be calculated based on motor performance and compared to the actual measured throat diameter. Each nozzle was measured pre and post-test using a coordinate measuring machine (CMM) that gathered highly accurate surface data. With that in mind, the theoretical values of C^* and C_F assume 100% efficiency, yet due to the poor combustion and instabilities, the actual efficiencies were found to be much lower. C^* typically averaged around 60 to 65 percent with C_F averaging between 100 and 115 percent. Figure 41 best illustrates the discrepancies between the modeled, measured, and theoretical values of C^* and C_F for the 2.07 MPa test case. Although not present, data from the 4.83 MPa and 3.45 MPa tests show very similar characteristics to those found in the 2.07 MPa test.

Here the measured values for C^* and C_F are calculated from measured thrust, chamber pressure, mass flow rate, and the original throat area. Whereas the back-calculated C^* and C_F are found with the NASA CEA Code by using the measured chamber pressure and O/F ratio. These calculations do not consider changes in throat diameter, therefore the throat area remains constant. Note, the back-calculations use the adjusted fuel properties discussed in the previous chapter. As a result of the large discrepancies between calculations and low combustion efficiency, C^* is not used to calculate the throat diameter as it is not truly representative of actual nozzle conditions. Thusly, throat area calculations were conducted using the thrust coefficient which aligned more closely to the modeled characteristics.

From there, Equation 7 is manipulated to solve for the transient throat area and throat diameter using the theoretical C_F gathered from the NASA CEA Code and the measured motor performance. Whereupon the transient throat diameter is differentiated to find the radial erosion rate and then compared to the measured throat erosion. The erosion is determined by calculating an effective throat diameter, wherein the circumference is used to find the throat radius and compare to the pre-burn nozzle diameter.

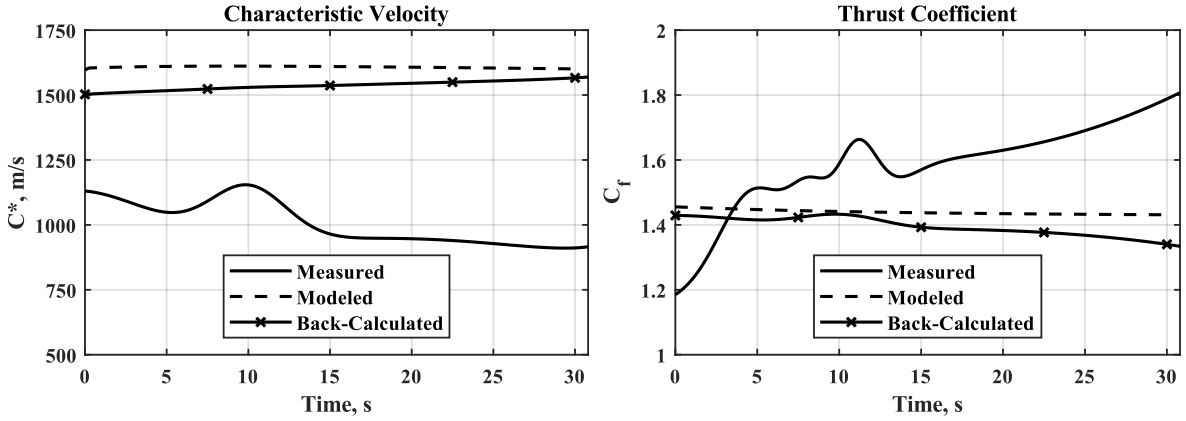

Figure 41. Comparison of the measured, modeled, and theoretical values for the characteristic velocity and the thrust coefficient during the 2.07 MPa test. Note that the theoretical C^* and C_F are approximated based on the O/F ratio during the test.

6.2 Nozzle Erosion: 2.07 MPa Test

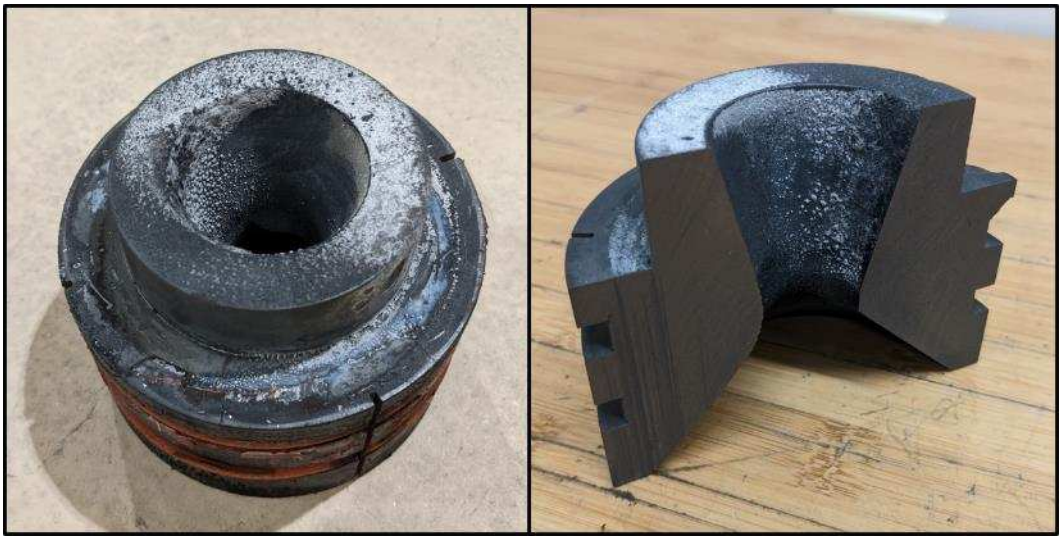

Figure 42. 2.07 MPa nozzle post-test fire.

Based on the analysis in Chapter 4 -, erosion is assumed to start 12 seconds after ignition when the thrust and chamber pressures transition from increasing to decreasing. The 2.07 MPa test resulted in a total radial erosion of 1.18 mm with a final throat diameter of 24.2 mm. Figure 43 shows the back-calculated throat diameter in addition to the total radial erosion and erosion rate after 12 seconds. It can be seen in the left most plot, the back-calculated transient throat diameter is considerably greater than that of the actual throat diameter, resulting from discrepancies between the theoretical and actual motor performance. Nonetheless, an accurate starting throat diameter is not critical, rather the change in throat diameter is.

Back-calculations resulted in a total radial erosion of 1.37 mm with an average erosion rate of 0.07 mm/s. This agrees well with the measured post-burn throat diameter of 1.18 mm, a difference of only 0.19 mm, or roughly the thickness of two sheets of paper. This indicates that the calculated erosion is likely representative of the actual erosion as well as correctly assuming that erosion started 12 seconds after ignition.

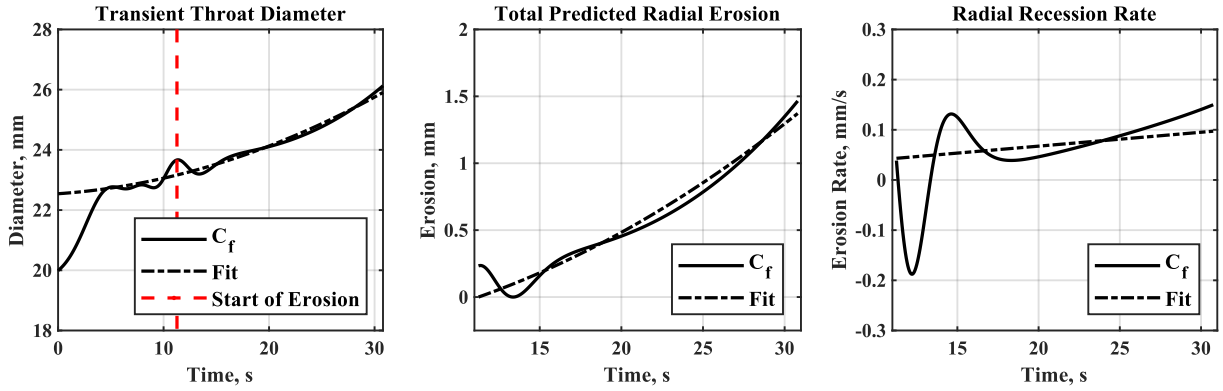

Figure 43. 2.07 MPa test plots of the back-calculated throat diameter (left), adjusted total radial erosion (center), and subsequent erosion rate (right). Total radial erosion assumes erosion starts at the transition point and therefore is zeroed at that point and only measuring the difference in throat diameter.

6.3 4.83 MPa and 3.45 MPa Nozzle Erosion

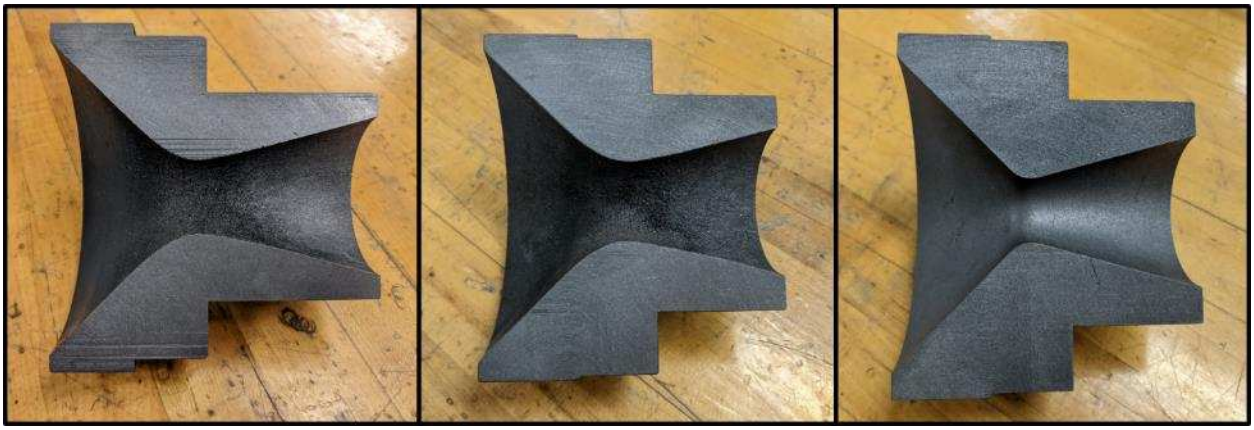

Figure 44. Photo set of the 4.83 MPa (left) and 3.45 MPa (center) posttest nozzle as well as a virgin nozzle on right.

Since the 4.83 MPa and 3.45 MPa tests share many of the same characteristics, the findings will be discussed in tandem. Beginning with the 4.83 MPa case, the measured radial erosion was 2.87 mm with a final throat diameter of 27.6 mm. Whereas the 3.45 MPa case resulted in 3.48 mm of erosion and a throat diameter of 28.8mm. Challengingly, these tests subvert the expectation that

higher chamber pressure results in higher erosion. Here, the lower 3.45 MPa test eroded nearly 1 mm more than the 4.83 MPa test.

Similar to Figure 43, Figure 45 and Figure 46 show the calculated radial erosion and erosion rate for the 4.83 MPa and 3.45 MPa tests. Importantly, these plots show the calculated erosion throughout the entire test to show the trends pre- and post-phase change. Moreover, the trendlines seen in Figure 45 and Figure 46 are piecewise defined polynomials that coincide at the point of phase change, hence the discontinuity in the erosion rate plots.

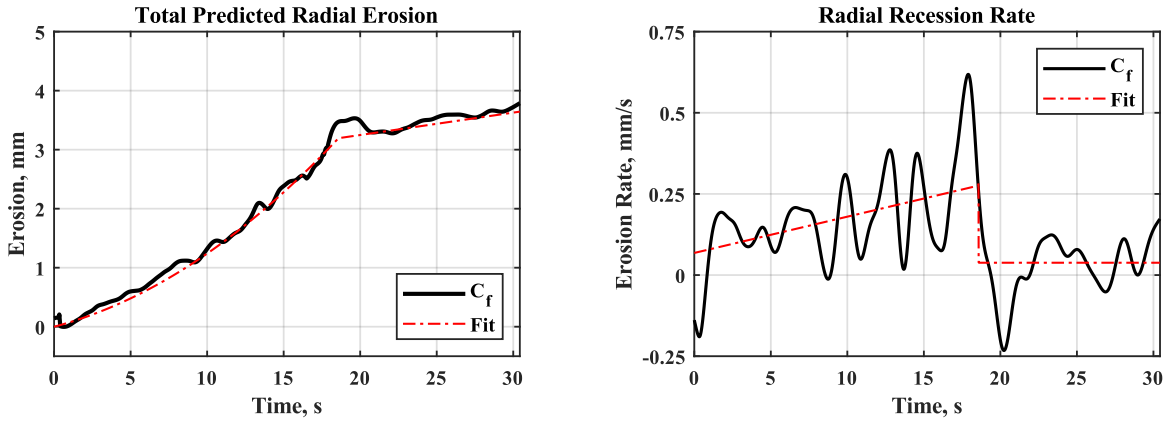

Figure 45. 4.83 MPa test plots of the adjusted total radial erosion (left) and subsequent erosion rate (right).

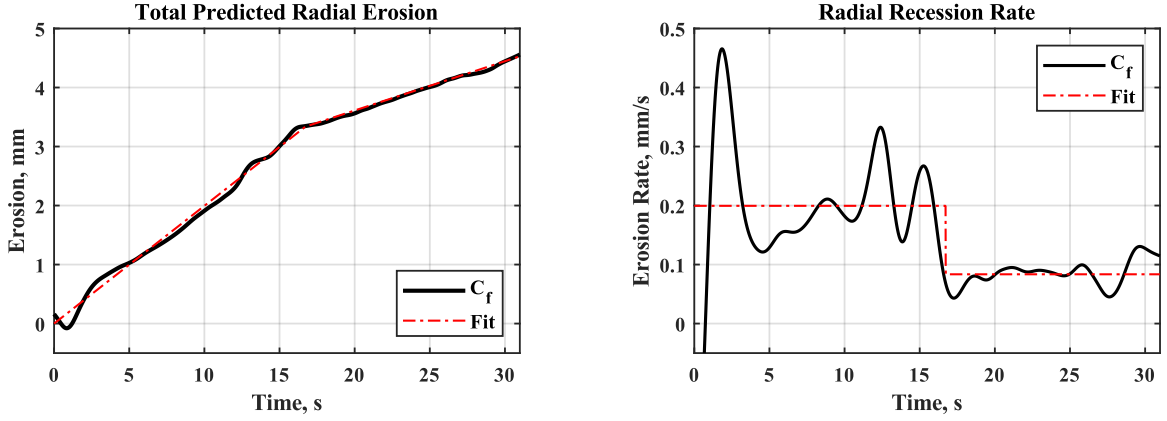

Figure 46. 3.45 MPa test plots of the adjusted total radial erosion (left) and subsequent erosion rate (right).

Ultimately, erosion can be calculated in one of two ways: where erosion begins immediately and stops at the point of phase change, or after the phase change when the nozzle temperature increases and the combustion stabilizes. Nevertheless, both assumptions have inherent drawbacks. The calculated pre-phase change radial erosion for the 4.83 MPa test was 3.19 mm, an over prediction of 0.32 mm, roughly 10% greater than the measured value. This ultimately leads to an average erosion rate of 0.17 mm/s, but calculations range anywhere from 0.07 mm/s to 0.27 mm/s. Post-phase change calculations, on the other hand, result in a total radial erosion of 0.44 mm, much lower than the actual nozzle, resulting in an average erosion rate of 0.07 mm/s. Regardless of reference frame, the calculated erosion does not adequately represent the true characteristics. Either the point where erosion starts is incorrect or the change in motor conditions had a much great effect erosion rates compared to the chamber pressure.

The 3.45 MPa test had many problems, yet the pre-phase change erosion calculations were substantially closer to the measured nozzle erosion. The total difference in radial erosion was 0.1 mm wherein the measured nozzle erosion was 3.48 mm, and the calculated erosion was 3.38 mm. In contrast, erosion calculations post-phase change under predicted erosion by 2.30 mm that averaged an erosion rate of 0.07mm/s.

Nonetheless, assuming erosion begins immediately after ignition is highly unlikely because the nozzle has yet to reach the reaction temperature. More likely, erosion occurred primarily after the phase change when the combustion instabilities subsided, thereby increasing combustion efficiency resulting in increased nozzle temperature and by extension the erosion rate. This is counter to what was measured, yet combustion efficiency cannot be directly calculated between the two halves of the test and as such the true conditions within the nozzle remain unknown.

6.4 Oxidizing Species

One the most important factors yet to be discussed is the role of oxidizing species present throughout the test fires. Because each motor ran oxidizer rich, concentrations of all oxidizing species were noticeably higher than the modeled predictions. Moreover, it has been shown that regardless of the oxidizer, oxidizer rich operation has a much more dramatic effect on erosion compared to fuel rich conditions [36]. It follows that the tests performed may have resulted in higher-than-expected erosion overall compared to the same motor operating under ideal conditions.

A good example, and the next highest concentration, is O_2. Although O_2 concentrations are still lower than H_2O and CO_2, oxygen requires much less energy to react with the carbon surface. O_2 consumes two carbon atoms from the surface rather than the one associated with H_2O and CO_2, effectively doubling the erosion. Comparisons between tested and modeled oxidizing species can be found in Figure 47. At first glance, it may not seem like the measured concentrations of oxidizing species presented in Figure 47 are greater than that of the model. But remember that the oxidizing species typically consumed during combustion, like O_2 and OH, are substantially more destructive, even in low quantities.

Secondly, the phase change experienced in the 4.83 MPa test, and the less noticeable change in the 3.45 MPa test, shifted the O/F ratio toward fuel rich, which would reduce erosion. The stark drop in oxidizing species related to the 4.83 MPa test is shown in Figure 47. Yet, as stated previously, the increase in nozzle temperature would lower the activation energy and increasing the reaction rate regardless of the O/F ratio. Moreover, the soot observed in the exhaust plum prior to phase change suggests the motors are running fuel rich at the start of the test, and are then transitioning to ideal or oxidizer rich combustion towards the end. This is all to illustrate the

inherent challenges and complexity associated with hybrid motor combustion. Because it's required for data analysis, it must be assumed that the motor operates at the measured O/F ratio, whereas in reality, the calculated concentrations of oxidizing species are likely not representative of the concentrations at the nozzle. For this reason, it is suspected that erosion increases after the phase change for both the 4.83 MPa and 3.45 MPa tests.

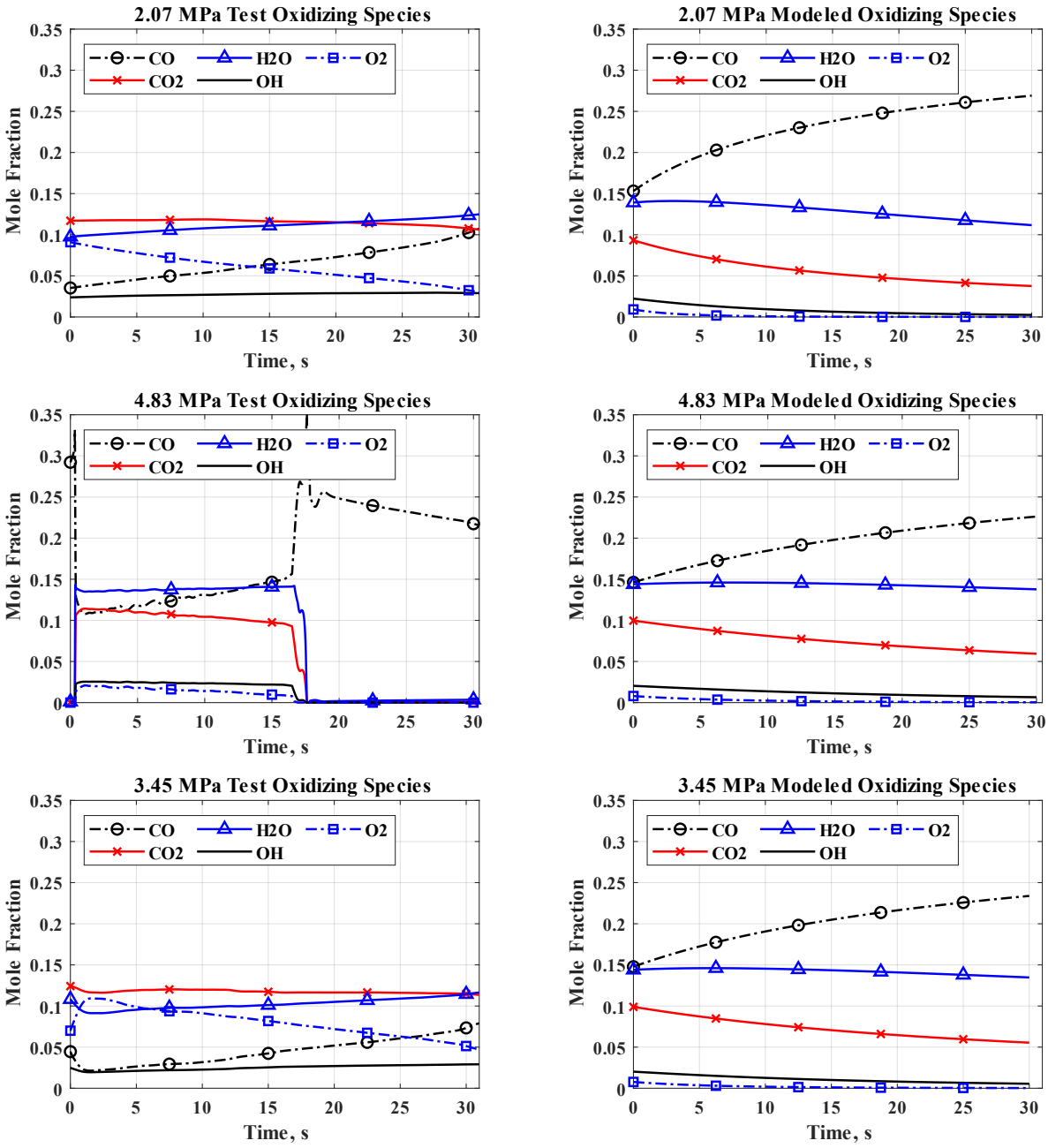

Figure 47. Collection of plots comparing the measured and modeled oxidizing species at the throat for each test case. Each row corresponds to the test case, starting with 2.07 MPa test on the first row moving downward to the 4.83 Mpa and 3.45 Mpa tests on the center and bottom row, respectively. The columns reference the measured species (left) and modeled species (right).

6.5 Chamber Pressure and Nozzle Erosion

Despite all the challenges discussed above, comparisons between this research and previous work can still inform the direction of future projects. To reiterate, the erosion prediction for the 2.07 MPa test aligned closely with the measured nozzle erosion, implying some level of accuracy to the calculated erosion rate of 0.07mm/s. More importantly, the 0.07 mm/s corresponds to an average chamber pressure of 1.37 MPa. That is, the average chamber pressure experienced during nozzle erosion. Table 12 compiles the corresponding chamber pressures and erosion rates for each test.

Table 12. Measured and calculated radial erosion as well as the associated erosion rates for each test. For the 4.83 MPa and 3.45 MPa test cases, the chamber pressure and erosion rates correspond to the averages pre and post phase change. Wherein, the left number refers to pre phase change and the right refers to post phase change.

Test Case	Average Chamber Pressure (MPa)	Measured Erosion (mm)	Calculated Erosion (mm)	Erosion rate (mm/s)
2.07	1.37	1.18	1.37	0.07
4.83	3.66 - 1.38	2.87	N/A	0.17 - 0.07
3.45	2.98 - 1.35	3.48	N/A	0.20 - 0.08

Table 12 also includes the average calculated erosion rates, both pre and post phase change, for the 4.83 MPa and 3.45 MPa tests. Remarkably, the post phase change chamber pressure from both tests averages around 1.37 MPa, the same average chamber pressure from the 2.07 MPa test. On top of that, all three tests result in an average erosion rate of 0.07 mm/s at 1.37 MPa. Since the erosion prediction from 2.07 MPa shows that the model is capable of accurately predicting erosion as function of changes in motor performance, it follows that the erosion rate at 1.37 MPa is likely near the calculated 0.07 mm/s, assuming the nozzle experiences similar exhaust gas and surface interacts.

As stated, the phase change during the 4.83 MPa and 3.45 MPa tests created a plethora of issues related to predicting total nozzle erosion. This largely stems from not being able to determine when erosion starts. Assuming the modeled erosion rates are reasonable, it follows that the model may be able produce approximate erosion rates when extrapolated to the other chamber pressures, specifically pressures experienced in the 4.83 MPa and 3.45b MPa tests prior to phase change. By doing so, calculations result in Figure 48.

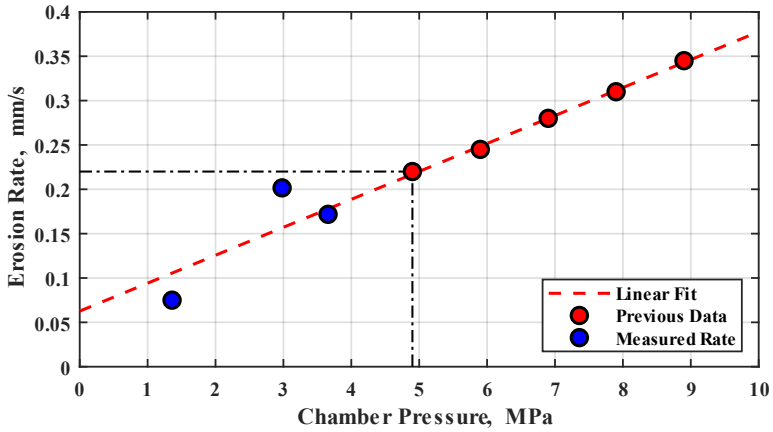

Figure 48: A compilation of the measured erosion rates in conjunction with previously gathered research data. The red data points and linearly fitted trendline correspond to the previously conducted research by Bianchi et al. 83[14].

In Figure 48, the predicted erosion rates similarly follow the linear fit previously established by Bianchi et al. (2009). While these predictions should be viewed with a grain of salt, the data gathered does support that non-linear boundary interactions play a lesser role than previously expected. At the same time, differences in chemical composition still play a large role in nozzle erosion and therefore require greater consideration. But if the linear relationship remains true, then the erosion rate of purely hydrocarbon fuels will simply have a steeper increase erosion rate compared to its solid rocket motor counterpart.

6.6 Nozzle Surface Profile

Finally, the gathered surface data illuminated unexpected erosion patterns, wherein two of the three nozzles eroded asymmetrically. Both the 2.07 MPa and 3.45 MPa tests experienced noticeably more erosion in a singular direction, with the 3.45 MPa test being the most extreme which eroded nearly 7mm greater than the rest of the nozzle. Interestingly, both nozzles eroded in similar directions. But unique to the 2.07 MPa test, erosion only occurred in only one direction, leaving the other side completely unaffected. Conversely, the 4.83 MPa nozzle, showed no signs of erosion irregularities, eroding uniformly around the entire surface despite having the highest instabilities and most extreme change in motor conditions.

The causes of asymmetric erosion still require more investigation; however, a combination of factors is suspected. Firstly, as the carbon is consumed the surface becomes rougher and more porous, subsequently increasing the surface area, leading to more reactions which increase erosion. As a result, a slight increase in surface roughness would likely act as a seed to further propagate the erosion in that direction. Likewise, if one half of the combustion chamber produces higher concentrations of oxidizing species, then the nozzle would also preferentially erode in that direction. This may be caused by uneven injector spray, where oxidizer preferentially travels down one side of the fuel grain, creating more oxidizing species in that area.

Figure 49 through Figure 51 show the gathered surface data from each of the nozzles with the origin in line with the longitudinal axis of the motor body. Additionally, the nozzles are measured such that the combustion products would be flowing from the top down. As a result, each motor showed more erosion toward the combustion chamber, which is to be expected because just upstream of the throat would have the smallest boundary layer and highest concentration of oxidizing species.

Figure 52 showcases both the surface roughness and preferential erosion found in the 2.07 MPa nozzle. Early revisions of the nozzle had much smaller radii leading into the throat and the throat was much larger in comparison. Due to the peculiar nature of the erosion, the 2.07 MPa nozzle cross-section shows both the unaffected and eroded portions of the nozzle simultaneously. The top edge of the throat shown in Figure 52 (left) has remained largely unaffected, in contrast to the bottom edge, which shows significant wear. The right photo in Figure 52 illustrates the increased surface roughness post testing. For context, the nozzle was polished to a high gloss finish prior to testing.

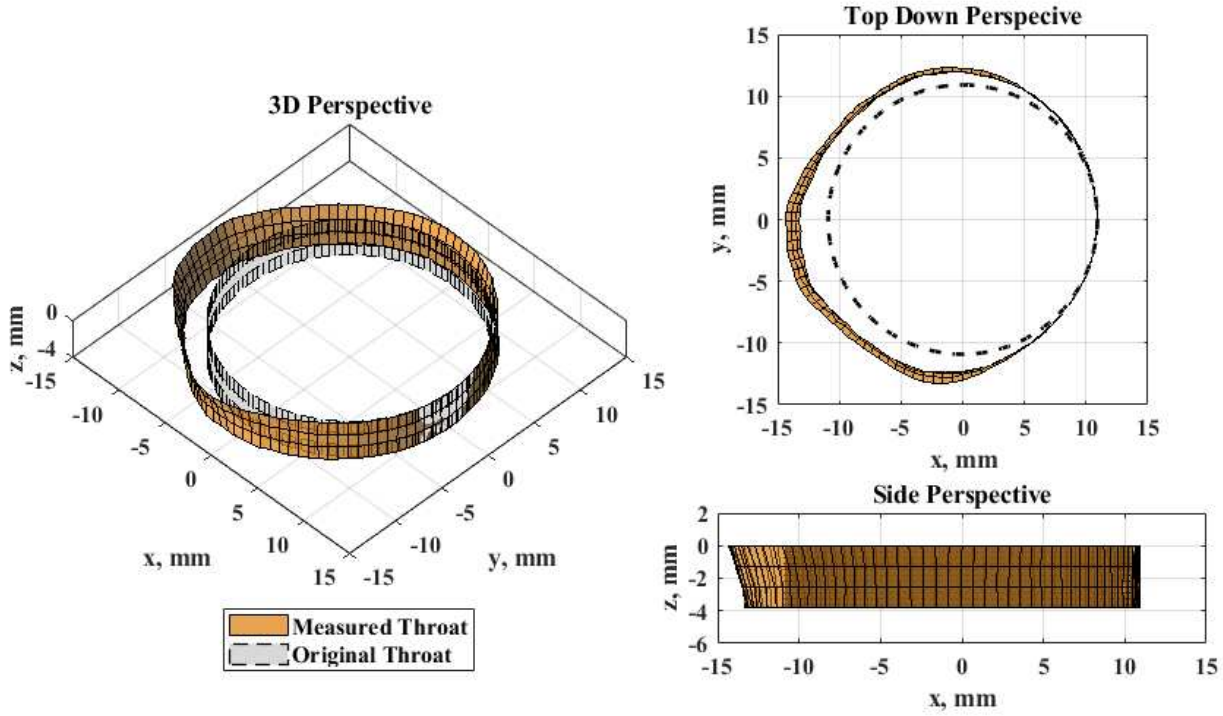

Figure 49. Nozzle surface data for the 2.07 MPa test with the axial center at (0,0) in addition to the x the y-axis in line with the true horizonal and vertical position of the nozzle during testing. The positive z-axis points toward the combustion chamber and negative axis point toward the nozzle.

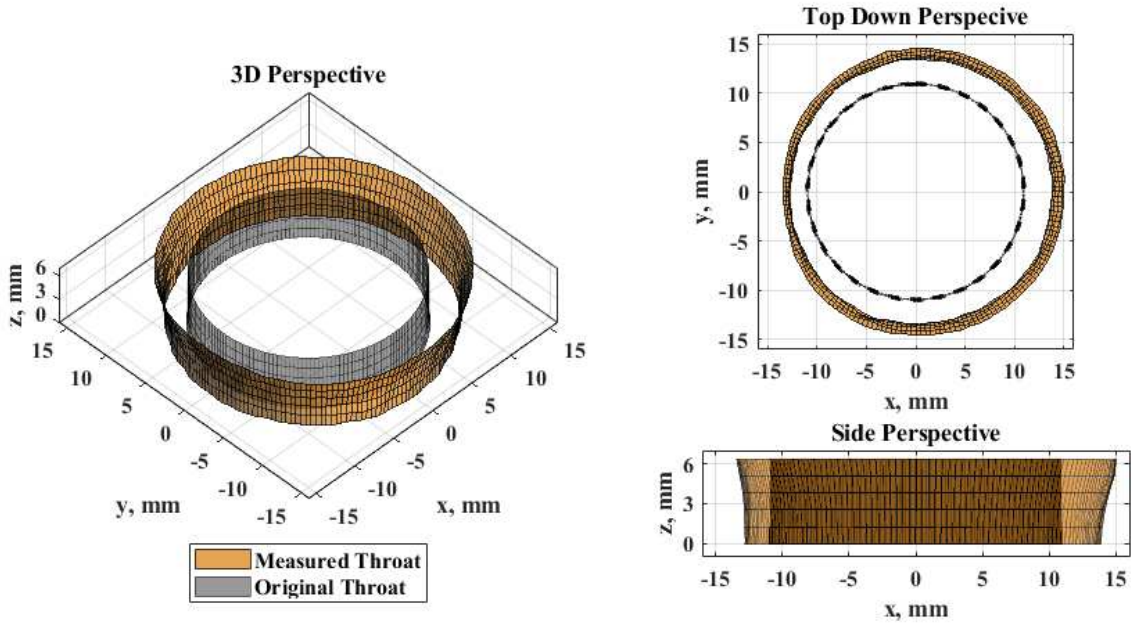

Figure 50. Surface meshes pre and post-test fire for the 4.83 MPa test.

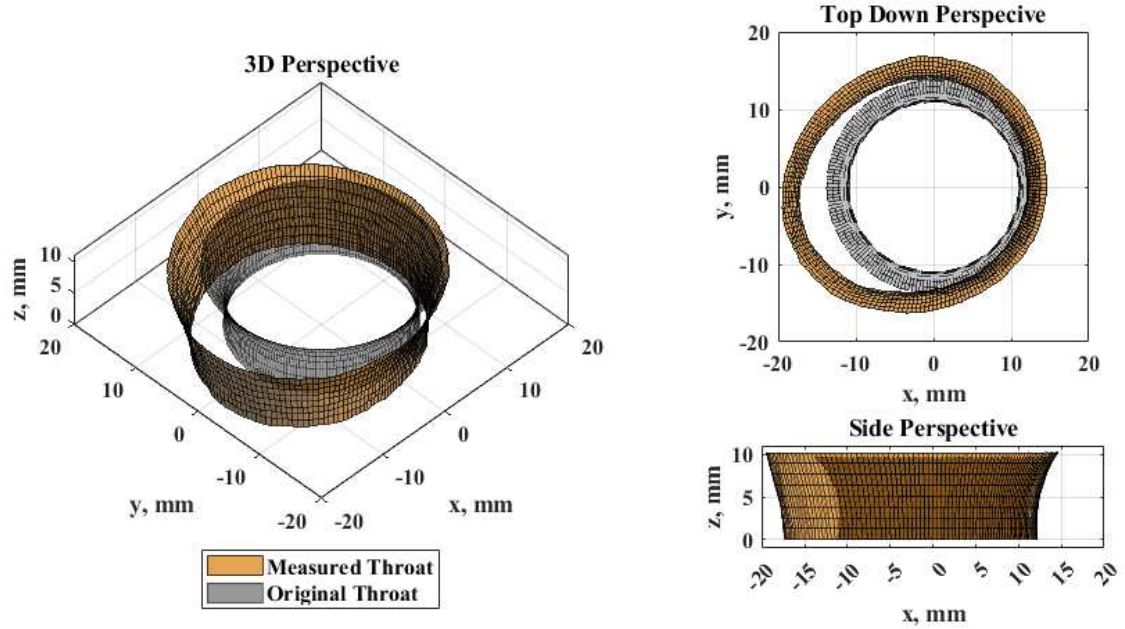

Figure 51. Surface meshes pre and post-test fire for the 3.45 MPa test.

Figure 52. Two perspectives, frontal cross-section (left) and close-up of the throat (right), of the nozzle post burn.

CHAPTER 7 - SUMMARY AND FUTURE WORK

In addition to correlating combustion chamber pressure to graphite nozzle erosion, much of this research included improving and constructing the infrastructure necessary for hybrid rocket motor development. Modeling was implemented to predict motor performance and construction, as well as to implement data analysis to predict nozzle erosion. The progress made from this project establishes the framework necessary to continue nozzle erosion research at Colorado State University.

The modernization and testing of the HRMTS demonstrates that data can be gathered safely and reliably for hybrid rockets operating in a wide range of conditions. Moreover, the calculations show that erosion can be predicted at low chamber pressures. This research illuminated the conditions at which erosion occurs and the potential that a linear relationship between chamber pressure and erosion rates remains valid at chamber pressures below 6.9 MPa.

While this work requires more development, continued testing could address the limitations in the HRMTS and testing procedure. Even more so, pursuing motor and injector design would not only resolve many of the issues arisen through this research, but help to validate other work focused on modeling hybrid rocket motor combustion. And finally, by resolving combustion instabilities more data can be collected to build on the foundation established through this work. With that in mind, some immediate changes that can be applied revolve around the oxidizer tank pressurization and combustion instabilities

7.1 Hybrid Rocket Motor Thrust Stand Limitations

Although the HRMTS has be shown to be capable for many situations, improvements can be made to address inadequacies in the nitrogen delivery. For all tests, the nitrogen back

pressurization was unable to maintain a constant oxidizer tank pressure during testing and therefore effected the oxidizer mass flow rate. Of course, some pressure changes are expected, especially those related to the decreased chamber pressure resulting from erosion, constant tank pressure would minimize upstream pressure fluctuation and the potential for phase change. As it stands the nitrogen system is designed for a max static pressure of 6.89 MPa, because of this, the dynamic pressure when pressurizing falls below the desired tank pressure.

Presently, the nitrogen system is only capable of delivering 4.14 MPa under ideal conditions. In some instances, this is less than the saturation pressure of the nitrous oxide thus guaranteeing a saturated fluid within the oxidizer lines, leading to cavitation and phase change prior to the injector. Simply increasing the static pressure capacity would increase the dynamic pressure allow the tank to maintain constant pressure during operation. This can also be solved during the design phase wherein the model would account for the drop in tank pressure and adjust the injector design accordingly. Hence, increasing the static line pressure limit would then allow for an increased dynamic pressure during operation.

7.2 Hybrid Motor Design Improvements

The next immediate update involves continued research regarding injector design, but more importantly, would involve improved fuel grain design. The current fuel grain design consists of two sharp 90-degree edges at either end of the grain. This likely results or contributes to post-fuel grain vortex shedding as well as combustion gas recirculation at the front of the fuel grain. As such, adding a taper to the entrance and exit of the fuel grain would help direct the flow around grain reducing vortices surrounding the fuel grain.

Additionally, the majority of nitrous oxide injector research stops at straight bore injector design. Other work has investigated specialized vortex or cavitating venturi injector designs, but simplified port geometries beyond straight bore ports have not been explored. Conical bores, with a port that tapers inward through injector port, would guarantee a length to diameter ratio to be less than one, regardless of the exit port diameter. Note, this design differs from a venturi injector as the taper would terminate at the face injector. Moreover, conical designs would likely increase the discharge coefficient by guiding the flow through the injector thereby reducing the time spent within the injector and reduce the change of phase change within the injector bore.

7.3 Liquid Rocket Motors

Overall, the best solution would involve continuing the development of the thrust stand and the transition to a liquid-liquid motor. The largest challenge throughout this project involved calculating the fuel mass flow rate. By moving to a liquid motor, the fuel mass can be directly measured, thereby reducing the number of unknowns and increasing the accuracy of the calculations. This does dramatically increase the complexity of the system and adds an increased level of risk. Nonetheless, the accuracy of the calculations would be greatly improved especially those related to concentration of oxidizing species.

REFERENCES

[1] Sutton, G., and Biblarz, O., Rocket Propulsion Elements, 9th ed., John Wiley & Sons, New York, 2017.

[2] Sundén, B., Fu, J., Heat Transfer in Aerospace Applications, 1st ed., Academic Press, 2017, Chaps. 2.

[3] Richter, G. P., and Smith, T. D., "Ablative Material Testing for Low-Pressure, Low-Cost Rocket Engines," NASA TM-107041, 1995.

[4] Turns, S. R., "An introduction to combustion: Concepts and applications, 3rd ed., McGraw-Hill, 2011.

[5] Keswani, S. T., Kuo, K. K., "Validation of an Aerothermochemical Model for Graphite Nozzle Recession and Heat-Transfer Processes," Combustion Science and Technology, Vol. 47, No. 3-4, 1986, pp. 177-192. doi: 10.1080/00102208608923872

[6] Klager, K. 1977, "The Interaction of the Efflux of Solid Propellants with Nozzle Materials," Propellants, Explosives, Pyrotechnics, Vol. 2, No. 3, 1977, pp. 55-63. doi: 10.1002/prep.19770020304

[7] Zhang, M., Yu Y., Xu, X., "A new flame sheet model to reflect the influence of the oxidation of CO on the combustion of a carbon particle," Combustion and Flame, Vol. 143, No. 3, 2005, pp. 150-158. doi: 10.1016/j.combustflame.2005.05.010

[8] Keswani, ST., Kuo K, K., "A Comprehensive Theoretical Model for Carbon-Carbon Composite Nozzle Recession," Combustion Science and Technology, Vol. 42, No. 3-4, 1985, pp. 145-164. doi: 10.1080/00102208508960374

[9] Thakre, P., Yang, V., “Chemical Erosion of Refractory-Metal Nozzle Inserts in Solid-Propellant Rocket Motors,” Journal of Propulsion and Power, Vol. 25, No. 1, 2009, pp. 40-50. doi: 10.2514/1.37922

[10] Delaney, L., Eagleton, L., Jones, W., "A semiquantitative prediction of the erosion of graphite nozzle inserts," AIAA 1964-102, Solid Propellant Rocket Conference, Jan 1964. doi: 10.2514/6.1964-102

[11] Shinn, A. M., “Experimental evaluation of six ablative-material thrust chambers as components of storable-propellant rocket engines,” NASA TN-D-3945, 1967.

[12] Bianchi, D., et al., 2012, “Naiver-Stokes analysis of scale effects on ablation in carbon-carbon rocket nozzles” Progress in Flight Physics, Vol. 3, 2012, pp. 382-394. doi: 10.1051/eucass/201203381

[13] Acharya, R., Kuo, K. K., “Effect of Pressure and Propellant Composition on Graphite Rocket Nozzle Erosion Rate,” Journal of Propulsion and Power, Vol. 23, No. 6, 2007, pp. 1242-1254. doi: 10.2514/1.24011

[14] Bianchi et al., “Coupled Analysis of Flow and Surface Ablation in Carbon-Carbon Rocket Nozzles,” Journal of Spacecraft and Rockets, Vol. 46, No. 3, 2009, pp. 492-500. doi: 10.2514/1.40197

[15] Kier, RJ., “An Investigation of Combustion Instability in Hybrid Rockets” NASA CR-155074, 1969.

[16] Thakre, P., Rawat, R., Clayton, R., “Mechanical Erosion of Graphite Nozzle in Solid-Propellant Rocket Motor,” Journal of Propulsion and Power, Vol. 29, No. 3, 2013, pp. 593-601. doi: 10.2514/1.B34630

[17] Thakre, P., Yang, V., 2008, "Chemical erosion of carbon-carbon/graphite nozzles in solid-propellant rocket motors," Journal of Propulsion and Power, Vol. 24, No. 4, 2008, pp. 822-833. doi: 10.2514/1.34946

[18] Browne, E., "Modeling Ablative and Regenerative Cooling Systems for An Ethylene/Ethane/Nitrous Oxide Liquid Fuel Rocket Engine," Master's Thesis, Mechanical Engineering Dept., Colorado State Univ., Fort Collins, CO, 2020.

[19] CEAC, Chemical Analysis and Equilibrium Code, Software Package, NASA, Cleveland, OH, 2005

[20] Netzer, D., Bae, W., "Hybrid Rocket Internal Ballistics" Chemical Propulsion Information Agency, Laurel MD, Jan. 1972.

[21] Marxman, G. A., Wooldridge, C. E., Muzzy, R. J., "Fundamentals of Hybrid Boundary-Layer Combustion," Progress in Astronautics and Rocketry, Vol 15. pp 485-522, 1964. doi: 10.1016/B978-1-4832-2730-6.50025-7

[22] Kuo, K. K., Lu, Y. C., Chiaverini, M. J., Harting, G. C., "Fundamental Phenomena on Fuel Decomposition and Boundary-Layer Combustion Processes with Applications to Hybrid Rocket Motors," NASA CR-197919, 1994.

[23] Marxman, G., Gilbert, M., "Turbulent boundary layer combustion in the hybrid rocket," Symposium (International) on Combustion, Vol. 9, No. 1, pp. 371-383, 1963. doi: 10.1016/S0082-0784(63)80046-6

[24] Cai, G., Zhang, Y., Tian, H., Wang, P., Yu. N., "Effect of grain port length–diameter ratio on combustion performance in hybrid rocket motors." Acta Astronautica, Vol. 128, 128 pp. 83-90, 2016. doi: 10.1016/j.actaastro.2016.07.002

[25] Wilde, J. P., “Fuel pyrolysis effects on hybrid rocket and solid fuel ramjet combustor performance,” PhD. Dissertation, Technical University of Delft, Delft, NL, 1991.

[26] Messineo, J., Lestrade, Y. Y., Hijlkema, j., Anthoine, J., “Vortex Shedding Influence on Hybrid Rocket Pressure Oscillations and Combustion Efficiency,” Journal of Propulsion and Power, Vol. 32, No. 6, 2016, pp 1386-1394. doi: 10.2514/1.B36049

[27] Fraters, A., Cervone, A., "Experimental characterization of combustion instabilities in high-mass-flux hybrid rocket engines." Journal of Propulsion and Power, Vol. 32, No. 4, 2016, pp 958-966. doi: 10.2514/1.B35485

[28] Doran, Eric, et al., 2007 "Nitrous oxide hybrid rocket motor fuel regression rate characterization," AIAA 2007-5352. 43rd AIAA/ASME/SAE/ASEE Joint Propulsion Conference & Exhibit. July 2007. doi: 10.2514/6.2007-5352

[29] Rocker, M., “Modeling of Nonacoustic Combustion Instability in Simulations of Hybrid Motor Tests,” NASA TP-2000-209905, 2000.

[30] Sanders, Isabelle C., et al., 2020 "Assessing Oxidizer Injector Design via Thermochemical Imaging of PMMA Combustion in a Hybrid Rocket Motor Geometry," AIAA 2020-3747. AIAA Propulsion and Energy 2020 Forum. August 2020. doi: 10.2514/6.2020-3747

[31] Carmicino, C., Russo, A. S., “Performance comparison between two different injector configurations in a hybrid rocket,” Aerospace Science and Technology, Vol. 11, No. 1, pp. 61-67, 2007. doi: 10.1016/j.ast.2006.08.009

[32] Gamper, E., and R. Hink., 2013, “Design and test of nitrous oxide injectors for a hybrid rocket engine.” Deutsche Gesellschaft für Luft-und Raumfahrt-Lilienthal-Oberth eV.

[33] Waxman, B. S., Zimmerman, J. E., “Mass Flow Rate and Isolation Characteristics of Injectors for Use with Self-Pressurizing Oxidizers in Hybrid Rockets,” AIAA 2013-3636. 49th AIAA/ASME/SAE/ASEE Joint Propulsion Conference. July 2013. doi: 10.2514/6.2013-3636

[34] Gany, A., Manheimer-Timnat, Y., Wolfshtein, M., “Two-phase flow effects on hybrid combustion,” Acta Astronautica, Vol 3, No 3–4, pp. 241-263, 1976. doi: 10.1016/j.ast.2006.08.009

[35] Invigorito, M., G. Elia, M. Panelli., 2016 "An improved approach for hybrid rocket injection system design," International Journal of Aerospace and Mechanical Engineering, 10, pp. 686-696.

[36] Bianchi, D., Nasuti. F., “Numerical Analysis of Nozzle Material Thermochemical Erosion in Hybrid Rocket Engines,” Journal of Propulsion and Power, Vol. 29, No. 3, 2013, pp. 547-558. doi: 10.2514/1.B34813